IN-VIVO PER-CUTANEOUS SINGLE FIBER REFLECTANCE SPECTROSCOPY OF HEPATIC STEATOSIS IN A RAT MODEL: QUANTITATIVE ASSESSMENT WITH RESPECT TO HISTOPATHOLOGY

By

NIGAR SULTANA

Bachelor of Science in Electrical, Electronic and Communication Engineering
Military Institute of Science and Technology
Dhaka, Bangladesh
2010

Submitted to the Faculty of the
Graduate College of the
Oklahoma State University
in partial fulfillment of
the requirements for
the Degree of
MASTER OF SCIENCE
May, 2015

IN-VIVO PER-CUTANEOUS SINGLE FIBER REFLECTANCE SPECTROSCOPY OF HEPATIC STEATOSIS IN A RAT MODEL: QUANTITATIVE ASSESSMENT WITH RESPECT TO HISTOPATHOLOGY

Thesis Approved:

Dr Daqing Piao

Adviser

Dr Kenneth E Bartels

Dr G. Reed Holyoak

Dr Jerry W Ritchey

ACKNOWLEDGEMENTS

I would like to thank my advisor Dr. Daqing Piao, for his support, encouragement and motivation throughout the entire way. I am especially thankful to him for standing beside me even in worst situations. It is his knowledge, patient input and enthusiastic discussion, which make this thesis work possible.

I would like to offer my gratefulness to the committee, Dr. Kenneth E. Bartels, Dr. G Reed Holyoak and Dr. Jerry W Ritchey for their valuable time in rat study, their encouragement and support in completing the work.

I am also thankful to my lab mates: Krishna Teja, Vasumathi Chalasani, Tristan Underwood and Tangfei Sun, for their discussion and comments on my results in improving my thesis.

Finally, I would like to thank my family. My heartiest thanks to my parents for believing on me and always being supportive. Without their enormous love and effort I could not reach this far.

This work is the result of a health research grant HR11-043 supported by the Oklahoma Center for the Advancement of Science and Technology (OCAST) and Kerr Foundation, Oklahoma City, OK to Dr. Bartels.

Acknowledgements reflect the views of the author and are not endorsed by committee members or Oklahoma State University.

Name: NIGAR SULTANA

Date of Degree: MAY, 2015

Title of Study: IN-VIVO PER-CUTANEOUS SINGLE FIBER REFLECTANCE SPECTROSCOPY OF HEPATIC STEATOSIS IN A RAT MODEL: QUANTITATIVE ASSESSMENT WITH RESPECT TO HISTOPATHOLOGY

Major Field: INTERDISCIPLINARY SCIENCE

Abstract: The assessment of hepatic steatosis has implications on liver transplantation. Reflectance spectroscopy using single fiber is a minimally-invasive technique applied to probing of biological tissues for extracting tissue optical properties. The aim of this study is to evaluate if per-cutaneous *in vivo* single fiber reflectance spectroscopy (SfRS) could identify steatotic liver from lean liver and if SfRS could assess the grading of lipid level accumulated in liver in a diet induced rat model. Twelve rats were separated to four in the control group that were fed normal diet and eight in the test group that were fed methionine-choline-deficient (MCD) diet. Percutaneous SfRS of the rat livers was performed under trans-abdominal ultrasound guidance and respiration gated data acquisition in day-0, day-13, day-27, day-41, and day-55. At each of the days of 13, 27, 41, and 55, one control rat and two test rats were euthanized after SfRS for collecting histopathology samples. The SfRS spectrum over 540-1000 nm was off-line processed for estimations of hemoglobin oxygen saturation, total hemoglobin concentration, lipid composition, effective scattering amplitude and power of the locally sampled liver parenchyma. Histopathology results of the twelve rats determined that all four control rats euthanized respectively on day 13, 27, 41 and 55 had insignificant lipid accumulation, two test rats euthanized on day 13 and another test rat euthanized on day 27 had mild lipid accumulation, one test rats euthanized on day 27 had moderate lipid accumulation, and four test rats, two test rats euthanized on day 41 and another two test rats euthanized on day 55 had severe lipid accumulation. SfRS results of the 4 rats originated in the control group and 8 test rats were compared and the steatotic livers shows a decreasing slope compares to normal liver. The total hemoglobin concentration also decreases as the lipid accumulation increases, starting $216.54 \pm 67.2\ 1\mu M$ in insignificant steatosis and ended up with $77.33 \pm 34.97 \mu M$ in severe steatotic liver. There is an increase in scattering amplitude and power, scattering power changed as 0.33 ± 0.0025 in insignificant, 34 ± 0.0030 for mild, 0.35 on moderate and 0.35 ± 0.0026 on severe steatotic liver at their respective days of euthanasia.

TABLE OF CONTENTS

Chapter Page

I. INTRODUCTION 1

1.1 Overview 1
1.2 Motivation 2
1.3 Literature review 3
1.4 Organization of report 5

II. BACKGROUND 7

2.1 Background of risk factors in liver transplantation 7
2.1.1 Liver transplantation without considering the quality of donor liver 7
2.1.2 Current clinical assessment method 8
2.1.3 Deficiencies of frozen biopsy for donor liver evaluation 8
2.1.3 The unmet clinical need in donor liver steatosis assessment 9
2.2 Single fiber reflectance spectroscopy 9
2.2.1 Introduction to single fiber reflectance spectroscopy 9
2.2.2 Normalization of reflectance spectrum 11
2.2.3 Choosing of references for normalization techniques used in studies 13
2.2.4 Mie theory 16

III. ANALYTICAL MODELING 20

3.1 Diffusion theory in radiative transfer 20
3.2 Reflectance in different medium geometry 23
3.2.1 Infinite medium 23
3.2.2 Semi-infinite medium 27
3.3 Relationship of scattering coefficient with reflectance in semi-infinite medium 30
3.4 Normalization methods 31
3.4.1 Intralipid and water based normalization 32
3.4.2 Air and water based normalization 33
3.4.3 Normalization with respect to reflectance standards and water 33
3.5 Mathematical characterization of normalized reflectance intensity and dependency on scattering properties 34

Chapter Page

3.5.1 Model comparison with MC simulation 34
3.5.2 Influence of fiber probing in tissue normalization....35
3.6 Validation of MC using liquid optical phantom 38
3.6.1 Intralipid phantom preparation 39
3.6.2 Normalization of liquid phantom....40

IV. MATERIALS AND METHODS 41

4.1 Diet and animal protocol....41
4.2 Single fiber reflectanse spectroscopy....44
4.2.1 Single fiber configuration for needle based probing of tissue 44
4.2.2 SfRS data acquisition and respiration gating implementation....45
4.2.3 Configuration for surface probing using diffuse reflectance standards ..41
4.3 Intralipid phantom preparation 42

V. RESULTS 48

5.1 Histological evaluation and steatosis grading....48
5.2 SfRS measurements performed on baseline and day of euthanasia....49
5.3 Scattering profile extraction....51
5.3.1 Scattering profile based on SfRS measurements 51
5.3.2 Scattering profile based on histology image analysis 52
5.4 Lipid concentration in rat liver 56
5.5 Total hemoglobin concentration 57
5.6 Scattering amplitude and scattering power 58

VI. CONCLUSION....60

6.1 Conclusion 60
6.2 Future works 62

REFERENCES 64

APPENDICES 72

LIST OF TABLES

Table Page

1.....44

LIST OF FIGURES

Figure Page

Fig 2.1 (a) raw spectral profile of source spectrum (b) The normalized reflectance spectra containing absorption and scattering profile at wavelength range 540-1000nm 12

Fig 2.2 Absorption coefficient of oxyhemoglobin (blue solid line), deoxyhemoglobin (red solid line), water (blue dashed line) and absorption coefficient of lipid (red dotted line) 15

Fig 2.3 (a) The normalized reflectance spectrum with respect to air and water (b) fitted spectrum $R_{norm}(\lambda)$ associated with normalized spectrum (red dashed line) and scattering profile (absorption decoupled from fitted spectrum) in blue dotted line 19

Fig 3.1 Photon emission and collection in infinite medium geometry using single fiber 24

Fig 3.2 Photon emission and collection in semi-infinite medium geometry using single fiber 27

Fig 3.3 (a) Normalization of semi-infinite probing using different references obtained from analytical model. (b) Results from MC simulation for single fiber reflectance vs dimensionless scattering 35

Fig 3.4 Reflectance vs dimensionless scattering for interstitial and surface probing normalized with respect to air and water 36

Fig 3.5 Reflectance vs dimensionless scattering for interstitial and surface probing normalized with respect to 20% intralipid and water 37

Fig 3.6 Reflectance vs dimensionless scattering for interstitial and surface probing normalized with respect to reflectance standards (99% and 2%) and water.....37

Fig 3.7 Reflectance vs dimensionless scattering from applying medium matched references for normalization 38

Figure Page

Fig 3.8 Reflectance intensity vs scattering coefficient at 632nm from air-water, intralipid-water and reflectance standards-water based normalization 40

Fig 4.1 The configuration for percutaneous SfRS of rat liver. Light source and spectrometer were coupled to a 200μm bifurcated fiber bundle (shown at top-left) to which a 320μm single fiber probe was connected. The single fiber probed into liver through a 20 gauge needle (schematic of angle polished fiber in needle shown at left), by ultrasound guidance (see the photograph in the middle panel). From the pneumatic pillow (covered by the rat and the small air tubing shadowed by the ultrasound cable), respiration of the rat was detected by a gating module for triggering the SfRS data acquisition (the triggering sequence is shown at the top right).....43

Fig 4.2 Schematic of Single fiber reflectance spectroscopy experimental setup.....45

Fig 4.3 Data acquisition interface. Air and water spectrum on first row, along with audio files plays upon starting the button to start taking spectrum. The adjustable threshold (blue slide swich on left side of rw two) used to generate Schmitt trigger depending on breathing signal (first image in row two) from respiration gating module and the SfR spectrum from sample liver (right corner of row two). Air and water based normalization of sample tissue shown at right side of first row 46

Fig 5.1 Photomicrograph of euthanized rats having (a) insignificant lipid accumulation, (b) mild lipid accumulation, (c) moderate lipid accumulation and (d) severe lipid accumulation 49

Fig 5.2 Comparison of the normalized SfRS measurements $R_{norm}(\lambda)$ from the baseline (left panel) to the respective days of euthanasia (right panel). The measurement from the rat originated from the control group is plotted as a solid black line. The measurements from the two rats in the test group are plotted as respectively dotted and dashed lines.....50

Fig 5.3 Steps to extract scattering profile from SfRS spectrum from rat liver 51

Fig 5.4 The normalized SfRS spectrum with respect to air and water (black solid line), fitted spectrum using equation to fit $R_{norm}(\lambda)$ (red dashed line) and scattering profile obtained from decoupling absorption out from $R_{norm}(\lambda)$ (blue dotted line) for (a) insignificant lipid accumulation, (b) mild, (c) moderate and (d) severe lipid accumulation.....52

Fig 5.5 Steps to extract scattering profile from histology image.....53

Fig 5.6 (a) Photomicrograph and (b) binary image with threshold 0.85.....53

Fig 5.7 Size distribution of lipid vacuoles from binary image, (a) insignificant steatotic liver, (b) mild, (c) moderate and (d) severe steatotic liver 54

Fig 5.8 Normalized SfRS spectrum with respect to air and water (black solid line), fitted spectrum using equation to fit $R_{norm}(\lambda)$ (red dashed line) and scattering profile obtained from decoupling absorption out from $R_{norm}(\lambda)$ (blue dashed line) where μ'_s obtained from photomicrograph analysis for (a) insignificant lipid accumulation, (b) mild, (c) moderate and (d) severe lipid accumulation 55

Fig 5.9 (a) Total area occupied by lipid vacuoles in microscopy images grouped by degree of lipid level, (b) measure SfRS normalized intensity grouped in degree of lipid level (green shows insignificant accumulation, black refers mild, blue refers moderate and red represents severe lipid accumulation) 56

Fig 5.10 Comparison of SfRS intensity for steatotic liver with lean liver euthanized on same day presented as: Column (1): "insignificant" was from a control rat scarified on day 13. Column (2): "mild" was from a test rat and insignificant from control rat both scarified on day 13 Column (3): "moderate" was from a test rat and insignificant from control those scarified on day 27. Column (4): "severe" was from a test rat scarified on day 55 along with insignificant from control rat 57

Fig 5.11 Total hemoglobin [HbT] of insignificant, mild, moderate and severe stetosis group measured at their day of euthanasia 58

Fig 5.12 (a) Scattering amplitude and (b) scattering power measured from insignificant, mild, moderate and severe stetosis group at their respective day of euthanasia.....59

CHAPTER I

TYPE TITLE HERE

1.1 Overview

In biomedical research, one of the most important challenges is to non-invasively characterize tissue properties through real time measurements for diagnosing of diseases or treatment purposes [1]. Single fiber Reflectance Spectroscopy (SfRS) is increasingly used for non-invasive and minimally invasive probing of biological tissues to determine tissue optical properties, which has a significant clinical implication [2]. Optical properties of tissue provide ample information regarding tissue macro-morphology and biochemical composition [3]. Such information can be used to describe tissue physiology, such as vascular oxygen saturation, blood volume, and cellular morphology, such as cell or organelle size and density [4-6]. Intensive studies have been performed using reflectance spectrum to diagnose diseases in various organs [7-9].

The aim of this study was to determine the feasibility of minimally invasive assessment of hepatic steatosis *in vivo* and quantifying the scattering amplitude and scattering power in an animal model using single fiber reflectance spectroscopy (SfRS). A single fiber is inserted percutaneously transabdominally into liver tissue to obtain tissue optical properties, which requires calibration of its reflectance spectrum. In this study, analytical modeling of single fiber reflectance spectroscopy normalization was developed. The model consists of both infinite and semi-infinite

medium geometry to show which normalization technique should be used depending on tissue probing condition, as there is no strict direction of which technique needs to be used while the fiber tip is place in contact with the hepatic surface or when the fiber is inserted inside into the tissue. The same normalization techniques are applied for different types of tissue probing without considering medium geometry. This work shows how normalization using respective geometry could provide correct information in acquiring tissue morphological and biochemical properties. Since SfRS measurement is highly sensitive to scatter size distribution, which allows this study to accurately sense the tissue scattering properties that agrees with simulated results from quantifying lipid droplets in histopathology images. This study was able to show how increasing lipid droplets in an animal model have significant influence on light scattering and the behavior of scatter size i.e., macro and micro steatosis in light scattering. The scattering spectrum obtained by decoupling the absorption spectrum from the normalized spectrum in the mentioned normalization technique provides information about scattering amplitude and scattering power, which was verified by the Mie-scattering from size-distribution of histopathology image.

1.2 Motivation

Liver transplant is the second most common transplant in the United States. In 2012 alone, 6256 liver transplants were performed in the United States and curently more than 17000 patients are on the active waiting list [10]. Every year, more than 1,500 people die waiting for a donated liver to become available. Discrepancies between the number of suitable liver donors and the increasing demand for transplantation compells the need to expand liver donor acceptance criteria, including consideration of organs of "marginal" quality, such as fatty livers from living or deceased donors [11]. Steatosis of the donor liver is a main risk factor for initial dysfunctional or non-functional grafs after transplant, since the fatty livers are particularly susceptible to ischemia reperfusion injury (IRI) [12]. Therefore assessment for the degree of steatosis of donor livers is a component of a succesful organ procurement program.

The motivation of this study was to assess hepatic steatosis in-vivo using single fiber reflectance spectroscopy (SfRS). The percutaneous reflectance spectroscopy performed on liver tissue provides information about tissue optical characteristics including absorption coefficient and reduced scattering coefficient. The analysis of optical properties indicates that the increasing scattering amplitude is related to an increase in fat vacuoles that assess how percutaneous SfRS measurement responds to hepatic steatosis in a needle-probing-compatible workflow which is the aim of the study.

1.3 Literature Review

Over several decades, single fiber reflectance spectroscopy has been studied for non-invasive probing of biological tissue. SfRS has the potential to assist clinicians in the selection of tissue extraction during standard biopsy procedures, and is applicable in tissues such as the breast, brain, and lymph nodes [3]. The majority of reflectance spectroscopy systems utilize multiple optical fibers to deliver and collect light during measurements, and the distance between the source and detector must be far enough for applying the theory of diffuse scattering [1,13]. Diffuse reflectance spectroscopy detects changes from a larger area and allows the light to penetrate deeper into the tissue which is desired for some applications, such as imaging breast or prostate [14, 15]. However, for other applications, a smaller source detector separation or even single fiber configuration is desired. Smaller source detector separation results in smaller probe size and usually simpler device design, making it more suitable for some medical uses, such as optical biopsy via endoscopy [16]. Reflectance signal results from elastic scattering within small local medium when the source and detector are located in close approximation. Other studies have shown the potential of distinguishing cancerous and noncancerous tissues by measuring the elastic scatter or fluorescence [1, 17]. For this study, single fiber configuration was used.

Reflectance spectroscopy studies were also performed with a single fiber configuration. The photon path length and sampling depth of single fiber reflectance has been simulated by Monte

Carlo Simulation and validated by phantom tests [18]. The potential for staging lung cancer using single fiber reflectance spectroscopy has also been demonstrated [19].

Normalization of reflectance spectra provides an important role in obtaining absorption and scattering coefficients as well as comparing tissue properties at specific wavelengths. Almost all reflectance spectroscopy related research has gone through this normalization process, using different samples for reference of normalization. The most commonly used samples for normalization process includes diffuse reflectance standards of high and low reflectivity, bulk intralipid of different concentrations, air and water. The combination referred to in various publications are water and 20% bulk intralipid [20-21], water and diffuse reflectance standard of high (99%) and low (2%) reflectivity [1, 2] and air and water [22-24] based normalization protocols.

However, none of these studies clearly defined which technique needs to be used while the fiber tip is place in contact with the surface or when the fiber is inserted into the tissue. To address this this issue a tissue medium geometry based normalization technique was proposed. As measurement geometry varies depending on tissue probing condition normalization techniques that follows the same geometry can be more efficient in determining tissue optical properties with accuracy.

Furthermore, liver functions have been effectively monitored by optical spectroscopy [25-32]. The conditions reported include absolute changes of oxyhemoglobin and deoxyhemoglobin [25, 26], endotoxemic shock in pig models wherein significant correlations were found between the perfusion parameters and the optical spectroscopy readings [30], intra-operative perfusion dynamics and oxygenation [31], etc. Optical spectroscopy is also valuable to quantifying lipid-infiltration in livers. Time-resolved NIR spectroscopy by Kitai et al [33] on excised livers of rats with different feeding regimens for inducing fatty changes of liver revealed lower absorption

coefficient (μ_a) and higher reduced scattering coefficient (μ_s') of fatty liver when compared to normal liver. The positive correlation between μ_s' and the lipid deposition indicated that fat droplets inside the hepatocyte were the dominant scatterers. Surface measurements on specimens of human liver by McLaughlin et al [33] also showed a correlation coefficient of 0.85 of the total diffuse reflectance intensity with the histologically identified lipid mass fraction of liver tissue.

Recently, diffuse reflectance spectroscopy has been performed on human liver both *in vivo* and *ex vivo* to assess hepatic steatosis [34]. The study reported a correlation of 0.854 between the histologic findings and DRS. Diffuse reflectance spectroscopy also showed a correlation 0.925 was between in vivo and ex vivo analysis for steatosis quantification.

To provide a technical solution to clinical challenges in distinguishing fatty liver from healthy normal liver, our study included the performance of SfRS to assess and quantify hepatic steatosis in-vivo. We report changes in optical properties due to accumulation of lipid droplets in liver over a designated period of time. The scattering amplitude and power were also correlated with fatty changes in liver compatible with scatter-size distribution.

1.4 Organization of Report

This thesis consists of two major areas of work. The first involved analytical modeling for normalization in infinite and semi-infinite medium geometry. This helps analyze the performance of normalization and further extends to model normalization of reflectance spectrum using different references that acts as different media. The second area involved single fiber reflectance spectroscopy (SfRS) performed on a diet nduced steatosis in a rat model.

This thesis is organized in six chapters: Chapter 2 reviews the risk to the outcome of liver transplant without considering degree of hepatic steatosis; the current clinical assessment methods and the need for a technological solution capable of real time monitoring and quantifying hepatic steatosis as well as a brief review of single fiber reflectance spectroscopy

(SfRS); the calibration of SfR spectrum in terms of normalization; why normalization is required and a review of different normalization techniques currently being used. In chapter 3, analytical modeling for normalization in infinite and semi-infinite medium is presented along with a model for normalization of reflectance spectrum with different references and comparisons of the model's performance are discussed. Chapter 4 provides the instrumentation and experimental setup. In Chapter 5, the experimental results from the rat study are presented. Chapter 6 provides conclusions and future work.

CHAPTER II

BACKGROUND

2.1 Background of risk factors in liver transplantation

2.1.1 Liver transplantation without considering the quality of donor liver

Liver transplantation is a therapeutic modality used for the treatment of end stage hepatic insufficiency. The result of transplantation depends on a healthy donor liver, which has an increased demand, although the supply of donor organ has not followed this demand [34]. The increased demand has led to the use of livers with marginal quality, such as steatotic livers [11]. Steatosis in deceased donor livers is the main risk factor for poor or non-function of the transplanted liver. It has also been associated with increased morbidity and mortality after resection. The size of fat vacuole determines the two microscopic categories of steatosis [11,36,37]: micro vesicular steatosis, when more than 90% of the lipid vacuole are smaller than the hepatocyte nucleus and macro vesicular steatosis, when a single large lipid droplet occupies most of the cell, displacing the cytoplasm and nucleus to a ring around the droplet. The degree of steatosis is graded semi-quantitatively [9]: no fatty change (<5%), mild (5 to 33%), moderate (33 to 66%) and severe (≥66%). Macrosteatosis in the donor organ represents a major risk to organ recipients with rates of primary non-function as high as 80% for severe steatosis and initial poor function as high as 30% in moderate steatotic organ [33]. Microsteatosis on the other hand, is not

associated with an increased risk of dysfunction. [37].

2.1.2 Current clinical assessment method

The clinical investigation of suspected steatosis includes blood testing, biopsy, Steatosis Test™ ultrasound (US), computed tomography (CT), magnetic resonance imaging (MRI) and magnetic resonance spectroscopy (^{1}H-MRS) [38-40]. Most of the imaging techniques, being non-invasive alternatives to liver biopsy, are poor at detecting and quantifying liver steatosis. The mean sensitivity estimates of these imaging techniques were 73.3-90.5% (US), 46.1-72.0% (CT), 82.0-97.4% (MRI) and 92.0-95.7% (^{1}H-MRS). Overall performance of MRI and ^{1}H-MRS was better than that for US and CT [41]. Therefore MRI and ^{1}H-MRS are usually considered imaging techniques of choice for evaluation of hepatic steatosis. However, they are time consuming and/or expensive, and impractical in some donor situations.

2.1.3 Deficiencies of frozen biopsy for donor liver evaluation

Despite its invasiveness the frozen-section liver biopsy remains the gold standard for the evaluation of hepatic steatosis [23]. Unfortunately, the conventional liver biopsy suffers from drawbacks, as detailed below, that hinder its utility in timely pre-operative evaluation of hepatic steatosis. First, the sampling error inherent in the conventional biopsy technique does not lend itself to representing tissue morphologies of multiple organ lobes. Secondly, the subjectivity in histopathology interpretation, especially with -Red-O sections [24], leads to a non-quantitative steatosis measure. Thirdly, even if the pathological interpretation were exact, the available time frame is limited and pathological resources are often unavailable in a transplant context. As a result, the surgeon's opinion of the degree of steatosis remains the most widely utilized assessment criterion. A yellowed appearance, rounded edges and stiff texture are judged to predict a suboptimal graft. Unfortunately, as many as 38% of organs, which were judged as normal by surgeons; showed steatosis upon biopsy [25].

2.1.4 The unmet clinical need in donor-liver steatosis assessment

A quantitative and instantaneous instrument for screening the intensity of steatosis, and further discriminating macro-steatosis from micro-steatosis, does not exists clinically [25]. Consequently, the tolerable steatosis threshold for successful transplantation outcomes is difficult to determine. Some organs with marginal degree of steatosis may be discarded inappropriately; others may be transplanted and result in non-function and even recipient death. A technological solution for quantitative donor-organ screening and assessment within the operating room is urgently needed, which would provide hepatic surgeons a reliable, immediate assessment of steatosis and discrimination of macrosteatosis from microsteatosis to maximize the number of usable donor organs.

2.2 Single fiber Reflectance Spectroscopy

2.2.1 Introduction to Single fiber Reflectance Spectroscopy

Single fiber Reflectance Spectroscopy (SfRS) is increasingly used for non-invasive and minimally invasive probing of biological tissues to determine tissue absorption and scattering coefficients, which have been shown to have clinical implications [2]. Tissues can be characterized by their optical properties, such as the absorption coefficients (μ_a) and reduced scattering coefficient (μ'_s), where $\mu'_s = \mu_s(1-g)$, g is the scattering anisotropy.

Reflectance spectroscopy is widely used in biomedical applications. Absorption of tissue depends on its biochemical structure and occurs at certain wavelengths whereas tissue scattering affects entire wavelength range associated with visible spectrum. The absorption coefficient obtained from reflectance spectroscopy contains the biochemical information of the tissue. Biological tissue chromophores, such as hemoglobin in its oxygenated and deoxygenated forms [41, 42],

melanin [7], bilirubin [43] and cytochromes [44], etc. are quantitatively assessed by measuring their absorption coefficient. On the other hand, scattering of light in tissue determines the ways of photon propagation within tissue and resulted from change in refractive index of tissue from surroundings. Scattering properties derived from reflectance spectroscopy convey the morphological characteristics of the biological tissues and could be related with the size and density of sub-cellular organelle [45, 46]. Reflectance spectroscopy has shown potential in diagnosing cancers or some precancerous lesions in various organs, such as colon [41], stomach [47], bladder [16], cervix [48], ovaries [49], breast [50, 51], brain [52], liver [53], heart [54], oral tissue [55] and skin [56].

Propagation of light in biological tissue is widely modeled using diffusion approximation [57-58]. However, diffusion approximation can be applied to two conditions: medium has to be scattering dominant, where scattering coefficient of tissue medium will be higher than absorption coefficient of that medium ($\mu'_s >> \mu_a$); and the separation between the source and detector needs to be large ($\rho >> 1/\mu'_s$).

At 500-950nm range of optical wavelength, scattering coefficient remains higher than absorption coefficient. However, the large source detector separation condition is not necessary to satisfy for all reflectance spectroscopy configurations. Diffuse reflectance measurements employ multiple source detector fibers, have long source collector fiber optical distances, and could reference large volumes. The large volume measurements of optical properties are desired in many applications, such as measurements in breast, prostate and other tissues. However, in some clinical cases, localized measurements are required, especially for operation during an interstitial procedure, in the surgical field or in small anatomical structures. Spatially constrained reflectance spectroscopy has been developed with small source collector fiber separation to address this need [58]. The source fiber delivers broadband light and the reflectance spectrum is detected by

collector fiber located at a distance, *r*, which could be very small from the source. A number of studies have been performed using a small source detector pair separation configuration, specifically for liver cancer diagnosis [59]. As an important parameter that influences the reconstruction of optical properties in a small source detector separation system, the separation distance between the source and detector fibers has been under intensive investigations [59-60].

Classical reflectance spectroscopy devices often utilize multiple optical fibers to deliver and collect light during measurement [61-62]; however, due to the advantages of reflectance probes with a single optical fiber to deliver and collect light, reflectance spectroscopy using single fiber has been studied here. Single fiber devices are advantageous over multi fiber due to their simplicity, compact design and small dimension [2]. The small probe size and simple design makes it more suitable than multi fiber probes for specific clinical applications [3]. Reflectance spectroscopy using single fiber has the potential to assist clinicians in the selection of tissue extraction during standard biopsy procedures, and is applicable in tissues such as the breast, brain, and lymph nodes [3]. While the hypodermic needle used for minimally invasive introduction into the abdominal cavity or other structure is often too small for multi- fiber probes to fit (with an inner diameter of only ≈ 400μm), this is not a concern for small single fiber probes with fiber diameters in the range of 200−400μm.

2.2.2 Normalization of reflectance spectrum

Reflectance spectroscopy using single fiber for both emission and collection of photons can be used to determine tissue optical properties, such as absorption coefficient (μ_a) and reduced scattering coefficient (μ'_s)). As the reflectance spectrum carries only a little information about tissue biochemical structure and micro morphology and only varies in intensity to each other, it is not sufficient to extract the optical properties from raw reflectance. Many clinical applications may require more localized measurement, other than information of bulk tissue properties only

[58]. Absorption and scattering occurs at different wavelength ranges and not visible in reflectance spectrum. Thus, comparing abnormal tissue from normal tissue may only show some change in intensity but not show how they differ in terms of light absorption and scattering. When the fiber tip is placed into a scattering medium, the measured spectrum contains not only the reflectance spectrum from the references, but also carries the base-line information due to use of a broadband light source which has a non-uniform spectral intensity profile referred as $S(\lambda)$. In order to decouple the internal-reflection and back reflection, as well as the source profile and spectrometer responsive characteristics from the measured spectrum, calibration of the spectrum is required. A normalization of raw reflectance spectra is performed for calibration with reflectance spectra from other references having known optical properties as

$$I(\lambda) = \frac{I_{tissue}(\lambda) - I_{reference2}(\lambda)}{I_{reference1}(\lambda) - I_{reference2}(\lambda)} \tag{1}$$

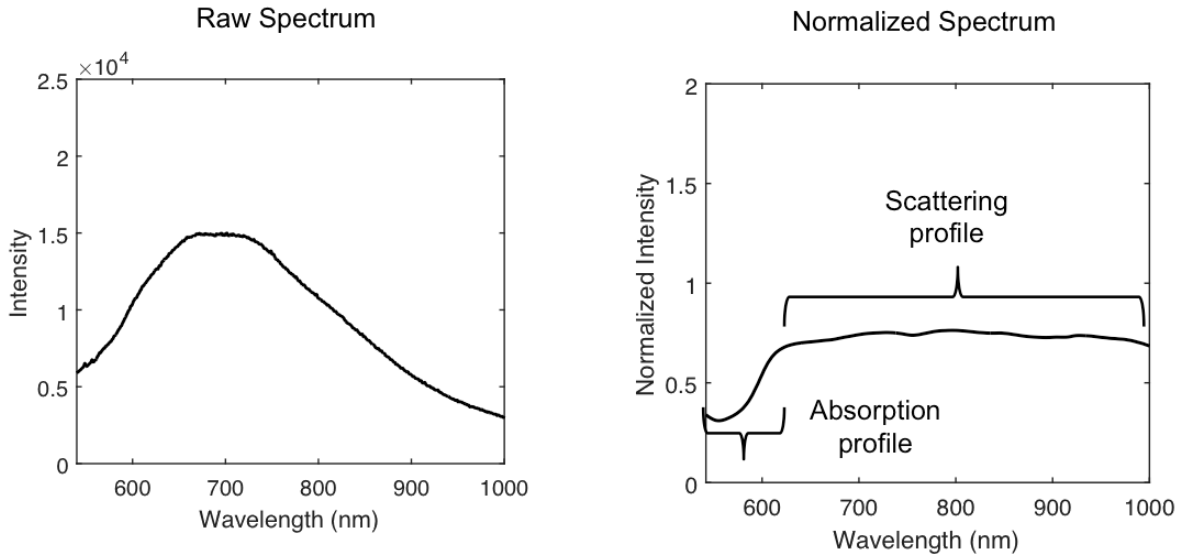

Figure 2.1: (a) raw spectral profile of source spectrum (b) The normalized reflectance spectra containing absorption and scattering profile at wavelength range 540-1000nm.

2.2.3 Choosing of references for normalization technique used in studies

Normalization of reflectance spectra provides an important role in obtaining absorption and scattering coefficients as well as comparing tissue properties at specific wavelength. Almost all the reflectance spectroscopy related research has gone through this normalization process, using different references for normalization. The most commonly used references for normalization process includes diffuse reflectance standards of high and low reflectivity, bulk intralipid of different concentrations, air and water. The combinations referred to various literatures are water and 20% bulk intralipid [20-21, 71],

$$I(\lambda) = \frac{I_{tissue}(\lambda) - I_{water}(\lambda)}{I_{\text{intralipid}}(\lambda) - I_{water}(\lambda)} \tag{2}$$

water and diffuse reflectance standard of high (99%) and low (2%) reflectivity [3-4]

$$I(\lambda) = \frac{I_{tissue}(\lambda) - I_{water}(\lambda)}{I_{99\%}(\lambda) - I_{2\%}(\lambda)} \tag{3}$$

And air and water [7, 13] based normalization

$$I(\lambda) = \frac{I_{tissue}(\lambda) - I_{water}(\lambda)}{I_{air}(\lambda) - I_{water}(\lambda)} \tag{4}$$

Regardless of the tissue probing geometry, the same normalization technique is applied in single fiber reflectance spectroscopy (SfRS). As measurement geometry varies depending on tissue probing condition, a normalization technique, which follows the same geometry, can be more effective in determining tissue optical properties with accuracy. Interstitial fiber probing follows infinite medium geometry where water and intralipid based normalization or air and water based normalization fits well as they both are having the same infinite medium geometry. Alternatively, water and diffuse reflectance standard based normalization presents a combination of infinite and

semi-infinite medium geometry, which works well if applied to semi-infinite geometry based probing on a tissue surface.

For this study, air and water were used as references. Due to the remnant specular reflection at the angle-polished fiber tip, both $I_{air}(\lambda)$ and $I_{water}(\lambda)$ contain the spectral profile $S(\lambda)$ but at different amounts, so the normalization using Eq. (1) gives rise to the following form [60],

$$R_{norm}(\lambda) = \xi \cdot \bar{R}_{scat}(\lambda) \cdot \exp\left\{-\mu_a(\lambda)\left\langle L(\lambda)\right\rangle\right\} \tag{5}$$

that is free of $S(\lambda)$, where $\xi = [\eta_{fib/air} - \eta_{fib/water}]^{-1}$, and $\eta_{fib/X}$ represents the specular reflection at the interface between the fiber and the respective medium "X". In Eq. (5) $\bar{R}_{scat}(\lambda)$ represents the contribution of tissue scattering to the SfRS signal in the absence of absorption, $\langle L(\lambda)\rangle$ represents the average pathlength of the photons detected by the fiber-probe. In arriving at Eq. (5), the refractive index of tissue is treated the same as that of water. Recent Monte Carlo (MC) simulations with experimental validations [3, 18, 20, 21] have suggested the following semi-empirical representations of $\bar{R}_{scat}(\lambda)$ and $\langle L(\lambda)\rangle$ when probed by a fiber of a diameter of d_{fib}:

$$\bar{R}_{scat}(\lambda) = \eta_{\lim}\left(1 + p_1 \exp\left[-p_3 \mu_s'(\lambda) d_{fib}\right]\right) \frac{\left[\mu_s'(\lambda) d_{fib}\right]^{p_2}}{p_3 + \left[\mu_s'(\lambda) d_{fib}\right]^{p_2}} \tag{6}$$

$$\left\langle L(\lambda)\right\rangle = \frac{p_4 \cdot d_{fib}}{\left[\mu_s'(\lambda) d_{fib}\right]^{p_5} \left\langle p_6 + \left[\mu_a(\lambda) d_{fib}\right]^{p_6}\right\rangle} \tag{7}$$

where $\eta_{\lim}$ is determined by the acceptance angle of the fiber and the refractive index difference between the medium and the fiber, and p_1 to p_6 are constants. The following sets of parameters are chosen, $p_1 = 0.63\gamma^2$, $p_2 = 0.57\gamma$, $p_3 = 2.31\gamma^2$, $p_4 = 1.05\gamma^{0.6}$, $p_5 = 0.18$, $p_6 = 0.64$

where $\gamma = 1.87$ for liver tissue is a parameter describing the effect of large angle scattering events on the reflectance signal, available with multi-diameter SfRS studies [20, 21, 60, 61]. The absorption coefficient is [18]

$$\mu_a(\lambda) = \left[\hat{\mu}_a^{OxyHb}(\lambda) StO_2 + \hat{\mu}_a^{DeoxyHb}(\lambda)(1 - StO_2)\right][Hb]_{total} \quad (8)$$

where $\hat{\mu}^{OxyHb}(\lambda)$ and $\hat{\mu}^{OxyHb}(\lambda)$ are respectively the absorption coefficients of $1\,\mu M$ oxyhemoglobin and $1\mu M$ deoxyhemoglobin (values exported from the spectral panel of Virtual Photonics [62]) (Fig 2), StO_2 is the hemoglobin oxygen saturation, $[Hb]_{Total}$ is the total hemoglobin concentration (in μM).

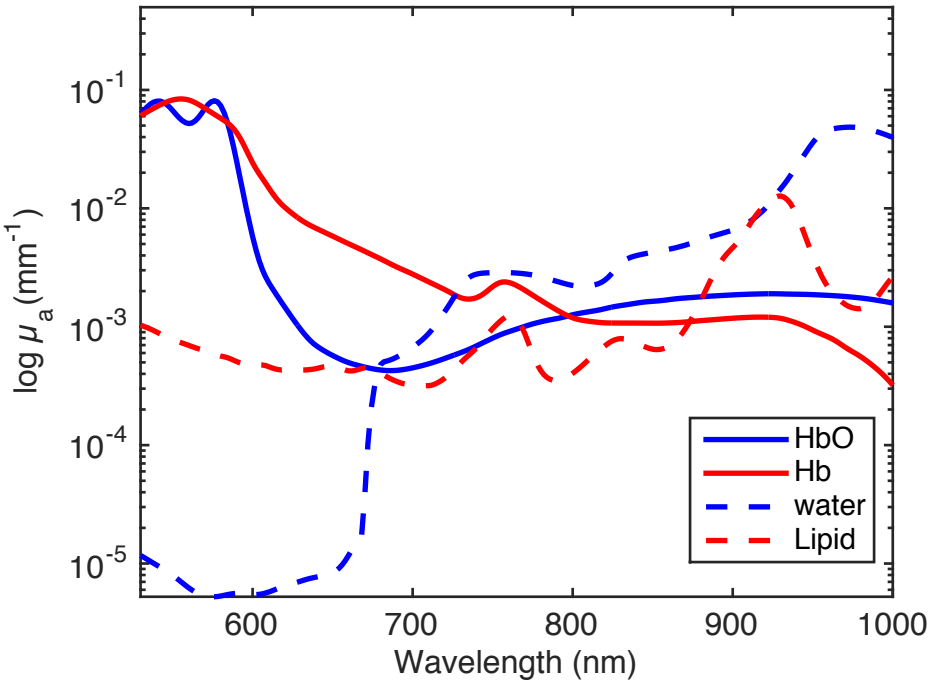

Figure 2.2: Absorption coefficient of oxyhemoglobin (blue solid line), deoxyhemoglobin (red solid line), water (blue dashed line) and absorption coefficient of lipid (red dotted line).

As the absorption coefficient of water and lipid is dominant at other wavelength range, and the SfRS normalized spectrum shows a high absorption only at the spectral range from 540-610nm, the absorption effect from water and lipid were not considered in this study. Total absorption coefficient is thus only associated with contribution from oxyhemoglobin, deoxyhemoglobin, hemoglobin oxygen saturation and total hemoglobin concentration. The scattering properties can be obtained using the Mie theory presented in the next section.

5.4.1 Mie scattering theory

The scattering of light can be explained by the electromagnetic wave theory and solved using Maxwell equation. The Mie theory is an analytical solution of the Maxwell equation for scattering of electromagnetic radiation by spherical particles.

For sphere particle of radius *r*, the scattering efficiency Q_{sca} (mm) and the scattering anisotropy factor *g,* are defined as [85]

$$Q_{sca} = \frac{2}{x^2}\sum_{l=0}^{\infty}(2l+1)(|a_l|^2 + |b_l|^2) \tag{9}$$

$$g = \frac{2}{Q_{sca}x^2}\left[\frac{l(l+2)}{l+1}\mathrm{Re}(a_l a_{l+1}^* + b_l b_{l+1}^*) + \frac{2l+1}{l(l+1)}\mathrm{Re}(a_l b_l^*)\right] \tag{10}$$

where $x = kr = \frac{2\pi n_b}{\lambda}r$, and n_b is the refractive index of the background medium. The coefficients a_l and b_l are given by,

$$a_l = \frac{\psi'_l(y)\psi_l(x) - n_{rel}\psi_l(y)\psi'_l(x)}{\psi'_l(y)\varsigma_l(x) - n_{rel}\psi_l(y)\varsigma'_l(x)} \tag{11}$$

$$b_l = \frac{n_{rel}\psi'_l(y)\psi_l(x) - \psi_l(y)\psi'_l(x)}{n_{rel}\psi'_l(y)\varsigma_l(x) - \psi_l(y)\varsigma'_l(x)} \tag{12}$$

where n_{rel} is the relative refractive index coefficient, $n_{rel} = \frac{n_s}{n_b}$, with n_S being refractive index of scatter, and $y = n_{rel}x = \frac{2\pi n_S r}{\lambda}$

$\psi(), \varsigma()$ are Riccati-Bassel functions and $\psi'(), \varsigma'()$ denote the first order derivative. The Riccatti-Bassel functions are defined by

$$\psi_l(z) = z j_i(z) = (\frac{\pi z}{2})^{1/2} J_{l+1/2}(z) \tag{13}$$

$$\chi_l(z) = -z y_l(z) = -(\frac{\pi z}{2})^{1/2} Y_{l+1/2}(z) \tag{14}$$

$$\varsigma_l(z) = \psi_l(z) + i\chi_l(z) = (\frac{\pi z}{2})^{1/2} H^{(2)}{}_{l+1/2}(z) \tag{15}$$

where *l* and *l+ 1/2* are the orders; $j_l()$ *and* $y_l()$ represent the spherical Bassel functions of the first and second kind, respectively; $J_l()$ *and* $Y_l()$ denote the Bessel functions of the first and second kind, respectively; $H^{(2)}_l$ Hankel function of the second kind. Here,

$$H_l^{(2)} = j_i() - i y_l() \tag{16}$$

the refractive index coefficients of background and scatters are wavelength dependent and can be expressed using Cauchy equations [86],

$$n(\lambda) = A + \frac{B}{\lambda} + \frac{C}{\lambda^2} \tag{17}$$

where *A, B, C* are constants for a certain material.

From the equations modeling the scattering efficiency Q_{sca} (mm^{-1}) and the scattering anisotropy factor *g*, we observed that for a particle, the scattering efficiency and scattering anisotropy are determined by its size and the relative refractive index coefficient between the particle and background.

Almost all scattering media consist of many particles of different sizes. If the particles are sparsely separate from each other, the scattering from other particles within the proximity of any particle is small. Additionally, if particle separation is random, there is no systematic relationship among the phase of waves scattered by the particles. With this single scattering assumption, the total scattering within the medium is simply the sum of scattering of all individual particles. For a scattering medium, the total cross section for scattering per unit volume, or the scattering coefficient, $\mu_s(\lambda)$ and the anisotropy coefficient $g(\lambda)$ for a suspension of particles with different radii can be calculated by [73]:

$$\mu_s(\lambda) = N_0 \sum_{i=1}^{n} \sigma_{sca}(r_i, \lambda) f(r_i) \tag{18}$$

$$g(\lambda) = \frac{\sum_{i=1}^{n} g(r_i, \lambda) \sigma_{sca}(r_i, \lambda) f(r_i)}{\sum_{i=1}^{n} \sigma_{sca}(r_i, \lambda) f(r_i)} \tag{19}$$

where, σ_{sca} is the scattering cross section and is calculated by

$$\sigma_{sca} = \pi r^2 Q_{sca} \tag{20}$$

$f(r_i)$ is the fraction of particles with radius ri and $\sum_{i=1}^{n} f(r_i) = 1$. N_0 is particle density given by

$$N_0 = \frac{v}{\sum_{i=1}^{n} \frac{4}{3} \pi r^3 f(r_i)} \tag{21}$$

where v is the volume of scatter per unit volume of suspension

The reduced scattering coefficient could be calculated by

$$\mu'_s(\lambda) = \mu_s(\lambda)(1 - g(\lambda)) \tag{22}$$

The μ_s' in Eq. (3) is further approximated by the power-law function of $\mu'_s(\lambda) = A\lambda^{-b}$ [68], where A is the scattering amplitude and b is the scattering power; the substitution of Eq. (3) into Eq. (2) leads to a new constant of $\eta_{eff} = \xi \cdot \eta_{\text{lim}}$. A nonlinear least-square fitting algorithm is applied for iterative estimation of the parameters of interest.

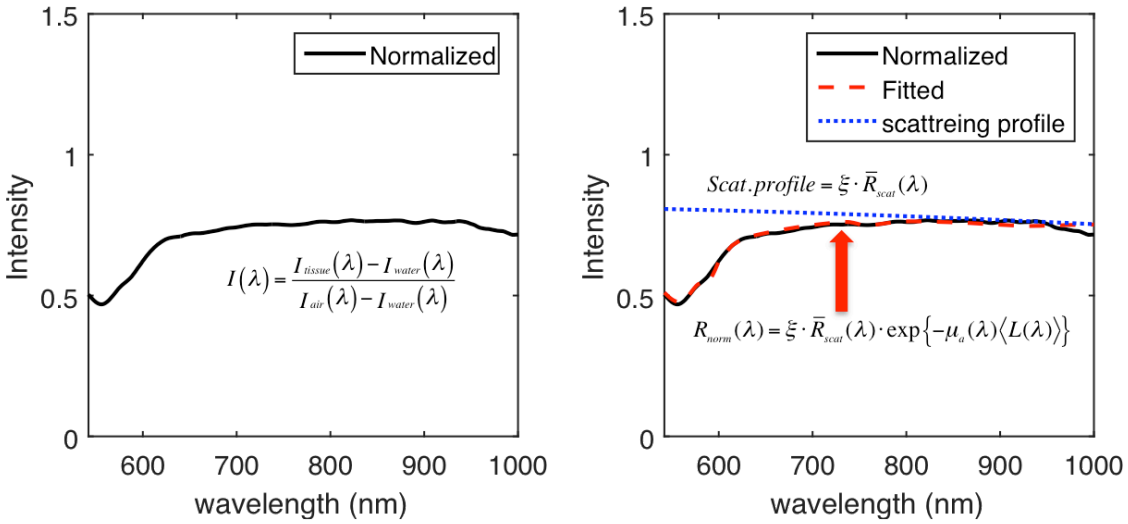

Figure 2.3: (a) The normalized reflectance spectrum with respect to air and water (b) fitted spectrum $R_{norm}(\lambda)$ associated with normalized spectrum (red dashed line) and scattering profile (absorption decoupled from fitted spectrum) in blue dotted line.

Fig 3(b) shows an estimated fit with respect to normalized spectrum in fig 3(a) using Eq. (2). The scattering profile is extracted by decoupling the absorption profile $\exp\{-\mu_a(\lambda)\langle L(\lambda)\rangle\}$ from Eq. (2), where $\mu_a(\lambda)$ and $\langle L(\lambda)\rangle$ estimated from using Eq. (5) and (4) respectively.

CHAPTER III

ANALYTICAL MODELING

In single fiber reflectance spectroscopy a single fiber is used for both delivering and collecting light to and from the medium. A single fiber design is advantageous over a multi-fiber design due to its simplicity and suitability in specific clinical applications [3]. In this chapter, total reflectance from medium either interstitially or surface probed using single fiber is analytically determined and then applied to a normalization method while probing matched references are used.

3.1 Diffusion theory in radiative transfer

The propagation of electromagnetic waves in scattering media can be described with the Boltzmann transport equation [73-76]

$$\frac{1}{c}\frac{\partial L(\vec{r},\hat{s},t)}{\partial t}+\nabla\cdot L(\vec{r},\hat{s},t)=-(\mu_s+\mu_a)L(\vec{r},\hat{s},t)+\mu'_s\iint_{4\pi}L(\vec{r},\hat{s}',t)P(\hat{s}'\cdot\hat{s})d\Omega'+S(\vec{r},\hat{s},t) \qquad (23)$$

where the radiance $L(\vec{r},\hat{s},t)$ has units (W/m2 sr) and where $\hat{s}$ is a unit vector pointing in the direction of interest.

The linear scattering and absorption coefficients, μ_s and μ_a, are the inverses of the mean free paths for scattering and absorption, respectively, and the normalized differential scattering cross section $P(\hat{s}'\cdot\hat{s})$ satisfies

$$\iint_{4\pi} P(\hat{s}' \cdot \hat{s}) d\Omega' = 1 \tag{24}$$

The source term $S(\vec{r}, \hat{s}, t)$ represents power injected into a unit solid angle centered on $\hat{s}$ in a unit volume at r.

Equation (24) above treats photons as billiard balls undergoing elastic collisions and traveling through the medium at speed c/n, where *n* is the refractive index of the medium (typically *n* = 1.40 for biological tissues).

Interference effects of photons are assumed to average to zero. In essence, the first equation provides a mathematical accounting of incoherent photons.

The similarity of transport equation to a continuity equation is emphasized by integration over all solid angles and use of the definitions of the fluence rate ϕ and the flux j**:**

$$\frac{1}{c}\frac{\partial \phi(\vec{r}, t)}{\partial t} + \nabla \cdot \vec{j}(r, t) = -\mu_a \phi(\vec{r}, t) + S(\vec{r}, t) \tag{25}$$

Where $\phi(\vec{r}, t) = \iint_{4\pi} L(\vec{r}, \hat{s}, t) d\Omega$ and

$\vec{j}(\vec{r}, t) = \iint_{4\pi} L(\vec{r}, \hat{s}, t) \hat{s} d\Omega$

When scattering is much stronger than absorption, the radiance can be expressed as an isotropic fluence rate 0 plus a small directional flux **j,** and transport equation reduces to a diffusion equation. [73-76]

$$L(\vec{r}, \hat{s}, t) = \frac{1}{4\pi}\phi(\vec{r}, t) + \frac{3}{4\pi}\vec{j}(\vec{r}, t) \cdot \hat{s} \tag{26}$$

Substituting this diffusion approximation and then multiplying by and integrating over all solid angles yields

$$\frac{1}{c}\frac{\partial \vec{j}(\vec{r}, t)}{\partial t} = -\frac{1}{3}\nabla \phi(\vec{r}, t) - \frac{1}{3D}\vec{j}(\vec{r}, t) \tag{27}$$

where $D = \frac{1}{3(\mu_a + \mu_s(1-g))}$, Dis the photon-diffusion coefficient; g is the average cosine of the scattering angle.

An additional assumption has considered that the source term S is isotropic. The steady state equation yields an expression for the flux analogous to Fick's law:

$$\vec{j}(\vec{r},t) = -D\nabla\phi(\vec{r},t) \tag{28}$$

Even when the source varies in time, it is a good approximation for biological tissues if the source frequencies are less than ~1 GHz.

The two relations between the fluence rate and the flux can be combined to yield a differential equation in the fluence rate alone as

$$D\nabla^2\phi(\vec{r},t) - \mu_a\phi(\vec{r},t) = (1+3D\mu_a)\frac{1}{c}\frac{\partial\phi(\vec{r},t)}{\partial t} - S(\vec{r},t) + \frac{3D}{c^2}\frac{\partial^2\phi(\vec{r},t)}{\partial t^2} - \frac{3D}{c}\frac{\partial S(\vec{r},t)}{\partial t} \tag{29}$$

For most biological tissues the scattering and absorption coefficients are in the range 10/cm < μ'_s < 50/cm and 0.03/cm < μ_a < 0.15/cm, so $3D\,\mu_a$ <<1. If the source varies in time with frequencies of less than ~1 GHz, then the last two terms in Eq. (15) can also be neglected, leaving the diffusion equation

$$D\nabla^2\phi(\vec{r},t) - \mu_a\phi(\vec{r},t) = \frac{1}{c}\frac{\partial\phi(\vec{r},t)}{\partial t} - S(\vec{r},t) \tag{30}$$

A solution to the diffusion equation for the simple case of a short-pulsed point source in an infinite homogeneous medium is presented here. The source term in the diffusion equation becomes $S(\vec{r},t,\vec{r}',t') = \delta(\vec{r}-\vec{r}')\delta(t-t')$, where $\vec{r}$ is the position at which fluence rate is measured and $\vec{r}'$ is the position of the source. The pulse peaks at time t'. The diffusion equation is solved for fluence rate to yield

$$\phi(\vec{r},t;\vec{r}',t') = \frac{c}{[4\pi Dc(t-t')]^{3/2}} \times \exp\left[-\frac{|\vec{r}-\vec{r}'|^2}{4Dc(t-t')} - \mu_a c(t-t')\right] \tag{31}$$

The term $\exp^{-\mu_a c(t-t')}$ represents the exponential decay in fluence rate due to absorption in accordance with Beer's law. The other terms represent broadening due to scattering. Given the above solution, an arbitrary source can be characterized as a superposition of short-pulsed point sources. Taking time variation out of the diffusion equation gives the following for a time-independent point source $S(\vec{r}) = \delta(\vec{r})$

$$\phi(\vec{r}) = \frac{1}{4\pi D}\frac{\exp(-kr)}{r} \tag{32}$$

$k_0 = \sqrt{\frac{\mu_a}{D}}$ is the effective attenuation coefficient and indicates the rate of spatial decay in fluence.

3.2 Reflectance in different medium geometry

In this section analytics associated with an infinite medium containing an equivalent isotropic source are derived. The total reflectance is determined by integrating the flux within the fiber. The analytics are then applied to the semi-infinite medium geometry, where boundary condition is considered.

3.2.1 Infinite medium

The figure below shows an infinite medium having effective attenuation coefficient, $k_0 = \sqrt{\frac{\mu_a}{D}}$ and diffusion coefficient, $D = \frac{1}{3(\mu_a + \mu'_s)}$, where μ_a and μ'_s are the absorption coefficient and reduced scattering coefficient respectively. Due to photon launching from a physical source to medium, into the medium an equivalent isotropic source is treated at $(0, z - R_a)$ where, $R_a = \frac{1}{\mu'_s}$.

The physical source- detector distance is ρ and the distance between equivalent isotropic source to detector is $l_{real} = \sqrt{\rho^2 + (z - R_a{}^2)}$ [77]

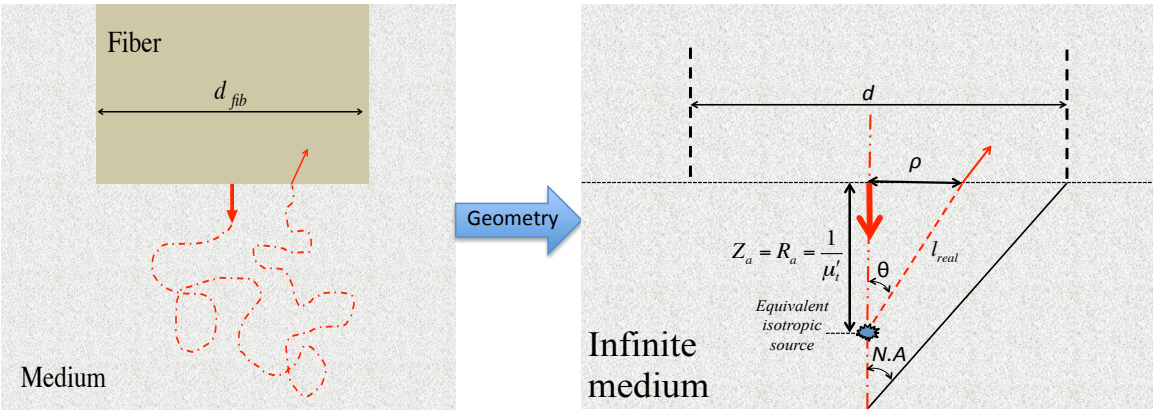

Figure 3.1: Photon emission and collection in infinite medium geometry using single fiber.

The photon fluence rate at (ρ,z) in infinite medium due to equivalent isotropic source at (0,R_a) is given by

$$\psi(\rho,R_a)=\frac{1}{4\pi D}\frac{\exp(-k0 l_{real})}{l_{real}} \tag{33}$$

Photons which leave the tissue at z = 0 after propagation represents the flux and flux at (ρ, R_a)is

$$R(\rho,R_a)=-D\nabla\psi(\rho,z)\big|_{z=0} \tag{34}$$

$$=-\frac{D}{4\pi D}\left[\frac{\sqrt{\rho^2+(z-R_a)^2}\exp\left(-k0\sqrt{\rho^2+(z-R_a)^2}\right)\frac{(-k0)2(z-R_a)(-1)}{2\sqrt{\rho^2+(z-R_a)^2}}-\exp\left(-k0\sqrt{\rho^2+(z-R_a)^2}\right)\frac{2(z-R_a)(-1)}{2\sqrt{\rho^2+(z-R_a)^2}}}{\left(\sqrt{\rho^2+(z-R_a)^2}\right)^2}\right]\Bigg|_{z=0}$$

$$=-\frac{1}{4\pi}\left[\frac{\exp\left(-k0\sqrt{\rho^2+(z-R_a)^2}\right)\frac{k0(z-R_a)}{\sqrt{\rho^2+(z-R_a)^2}}+\exp\left(-k0\sqrt{\rho^2+(z-R_a)^2}\right)\frac{(z-R_a)}{\sqrt{\rho^2+(z-R_a)^2}}}{\left(\sqrt{\rho^2+(z-R_a)^2}\right)^2}\right]\Bigg|_{z=0}$$

$$= \frac{1}{4\pi}\left[\frac{R_a \exp\left(-k_0\sqrt{\rho^2+R_a^2}\right)}{\left(\sqrt{\rho^2+R_a^2}\right)^2}\left(k_0+\frac{1}{\sqrt{\rho^2+R_a^2}}\right)\right]$$

The total diffuse reflectanceR_ρ that is the total number of photons collected by detector can be calculated by integrating radially dependent diffuse reflectance over the entire infinite medium as

$$R_\rho(R_a) = \int_0^\infty R(\rho, R_a) 2\pi\rho d\rho$$

$$= \frac{2\pi}{4\pi}\int_0^\infty \rho\left[\frac{R_a \exp\left(-k_0\sqrt{\rho^2+R_a^2}\right)}{\left(\sqrt{\rho^2+R_a^2}\right)^2}\left(k_0+\frac{1}{\sqrt{\rho^2+R_a^2}}\right)\right]d\rho$$

Let, $v = \dfrac{\exp\left(-k_0\sqrt{\rho^2+R_a^2}\right)}{\sqrt{\rho^2+R_a^2}}$

$$\Rightarrow dv = \frac{1}{\left(\sqrt{\rho^2+R_a^2}\right)^2}\left[\sqrt{\rho^2+R_a^2}\left\{k_0\exp\left(-k_0\sqrt{\rho^2+R_a^2}\right)\frac{2(-k_0)\rho}{2\sqrt{\rho^2+R_a^2}}\right\} - k_0\exp\left(-k_0\sqrt{\rho^2+R_a^2}\right)\frac{2\rho}{2\sqrt{\rho^2+R_a^2}}\right]$$

$$= \frac{1}{\left(\sqrt{\rho^2+R_a^2}\right)^2}\left[-k_0^2\rho\exp\left(-k_0\sqrt{\rho^2+R_a^2}\right) - \frac{k_0\rho}{\sqrt{\rho^2+R_a^2}}\exp\left(-k_0\sqrt{\rho^2+R_a^2}\right)\right]$$

$$= \frac{-k_0\rho}{\left(\sqrt{\rho^2+R_a^2}\right)^2}\exp\left(-k_0\sqrt{\rho^2+R_a^2}\right)\left(-k_0+\frac{1}{\sqrt{\rho^2+R_a^2}}\right)$$

$$u = -\frac{1}{k_0} \qquad \Rightarrow du = 0$$

$$\int u dv = uv - \int v du$$

$$\Rightarrow \frac{1}{2} R_a \int_0^{\infty} \frac{\rho}{\left(\sqrt{\rho^2 + R_a{}^2}\right)^2} \exp\left(-k_0 \sqrt{\rho^2 + R_a{}^2}\right)\left(-k_0 + \frac{1}{\sqrt{\rho^2 + R_a{}^2}}\right) d\rho = -\frac{1}{2} R_a \left[\frac{\exp(-k_0 \sqrt{\rho^2 + R_a{}^2}}{\sqrt{\rho^2 + R_a{}^2}}\right]_0^{\infty}$$

$$= \frac{1}{2}\left[\exp(-k_0 R_a)\right]$$

For determining the photons collected by fiber, radially dependent diffuse reflectance is integrating over the fiber diameter as

$$R_\rho(R_a) = \int_0^{\rho} R(\rho, R_a) 2\pi\rho d\rho$$

$$= \frac{1}{2} \int_0^{\rho} \rho \left[\frac{R_a \exp\left(-k_0 \sqrt{\rho^2 + R_a{}^2}\right)}{\left(\sqrt{\rho^2 + R_a{}^2}\right)^2}\left(k_0 + \frac{1}{\sqrt{\rho^2 + R_a{}^2}}\right)\right] d\rho$$

$$= \frac{1}{2} R_a \left[-\frac{\exp(-k_0 \sqrt{\rho^2 + R_a{}^2}}{\sqrt{\rho^2 + R_a{}^2}}\right]_0^{\rho}$$

$$= \frac{1}{2}\left[\exp(-k_0 R_a) - \frac{R_a \exp(-k_0 \sqrt{\rho^2 + R_a{}^2})}{\sqrt{\rho^2 + R_a{}^2}}\right]$$

3.2.2 Semi-infinite medium

Figure 3.2 shows the semi-infinite medium geometry with the physical source and detector located at the boundary. The physical point source launches the photon into the medium at an initial direction orthogonal to the medium–applicator interface, and is treated as an equivalent "real" isotropic point source located one step of transport scattering, $R_a = {}^{1}/_{\mu'_s}$, into the medium [74]. The "real" isotropic source has the coordinate$(0, z - R_a)$for the origin at the medium side. The effect of the medium–applicator interface on photon diffusion at the excitation wavelength may be modeled by an extrapolated zero-boundary condition [78-81], which sets zero Ψex at an imaginary boundary located R_b = 2AD off the physical boundary, where A=$\frac{1+r_d}{1-r_d}$ and r_d is a coefficient [74, 78] determined by the refractive index differences across the physical boundary. This extrapolated zero-boundary condition is accommodated by setting a sink or a negative "image" of the "real" isotropic source, with respect to the extrapolated boundary. The "image" source has the strength of the "real" isotropic source, and locates at (0, z+R_a+2R_b), for the origin at the medium side. Then on the extrapolated boundary Ω the following condition is satisfied:

$$\psi^{ex}_{semi}(\vec{r}) = \psi^{ex}_{\inf}(\overrightarrow{l_{real}}) - \psi^{ex}_{\inf}(\overrightarrow{l_{img}}) = 0 \tag{35}$$

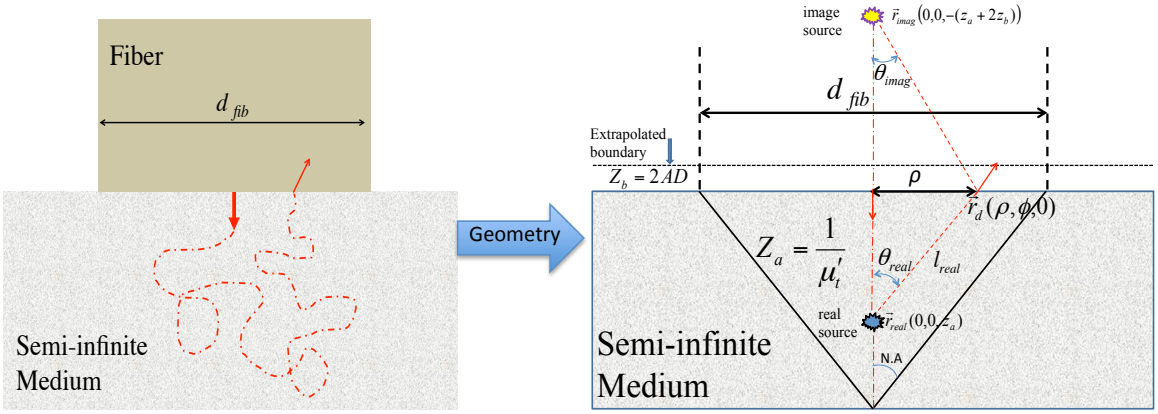

Figure 3.2: Photon emission and collection in semi-infinite medium geometry using single fiber.

The distances from the "real" isotropic source and its "image" to the detector at $\vec{\rho}$ are denoted by $r_r = \sqrt{\rho^2 + (z - R_a)^2}$ and $r_i = \sqrt{\rho^2 + (z + R_a + 2R_b)^2}$, respectively. The straight-line distance between the physical source and the detector, ρ, is referred to as the "line-of-sight"source–detector distance. The fluence at (ρ,z) in infinite medium due to real source at $(0, R_a)$ and image source at (0, $-2R_b - z_0$) is

$$\psi(\rho, R_a) = \frac{1}{4\pi}\left[\frac{\exp(-k_0 r_r)}{r_r} - \frac{\exp(-k_0 r_i)}{r_i}\right] \tag{36}$$

The photons which leaves the tissue at z = 0 after propagation represents the flux at(ρ, R_a), whichis given by

$$F(\rho, R_a) = -D\nabla\psi(\rho, z)\Big|_{z=0}$$

$$= -\frac{1}{4\pi}\left[\begin{array}{l} \dfrac{\exp\left(-k_0\sqrt{\rho^2+(z-R_a)^2}\right)\dfrac{k_0(z-R_a)}{\sqrt{\rho^2+(z-R_a)^2}} + \exp\left(-k_0\sqrt{\rho^2+(z-R_a)^2}\right)\dfrac{(z-R_a)}{\sqrt{\rho^2+(z-R_a)^2}}}{\left(\sqrt{\rho^2+(z-R_a)^2}\right)^2} \\ -\dfrac{\exp\left(-k_0\sqrt{\rho^2+(z+R_a+2R_b)^2}\right)\dfrac{-k_0(z+R_a+2R_b)}{\sqrt{\rho^2+(z+R_a+2R_b)^2}} + \exp\left(-k_0\sqrt{\rho^2+(z+R_a+2R_b)^2}\right)\dfrac{(z+R_a+2R_b)}{\sqrt{\rho^2+(z+R_a+2R_b)^2}}}{\left(\sqrt{\rho^2+(z+R_a+2R_b)^2}\right)^2} \end{array}\right]_{z=0}$$

$$= \frac{1}{4\pi}\left[\frac{R_a\exp\left(-k_0\sqrt{\rho^2+R_a{}^2}\right)}{\left(\sqrt{\rho^2+R_a{}^2}\right)^2}\left(k_0 + \frac{1}{\sqrt{\rho^2+R_a{}^2}}\right) + \frac{(R_a+2R_b)\exp\left(-k_0\sqrt{\rho^2+(R_a+2R_b)^2}\right)}{\left(\sqrt{\rho^2+(R_a+2R_b)^2}\right)^2}\left(k_0 + \frac{1}{\sqrt{\rho^2+(R_a+2R_b)^2}}\right)\right]$$

The total diffuse reflectanceR_ρ that is the total number of photons collected by detector can be calculated by integrating radially dependent diffuse reflectance over the entire infinite medium as

$$R_\rho(R_a) = \int_0^\infty R(\rho, R_a) 2\pi\rho d\rho$$

$$= \frac{1}{2}\int_0^\infty \rho \left[\frac{R_a \exp\left(-k_0\sqrt{\rho^2+R_a^2}\right)}{\left(\sqrt{\rho^2+R_a^2}\right)^2}\left(k_0+\frac{1}{\sqrt{\rho^2+R_a^2}}\right) + \frac{(R_a+2R_b)\exp\left(-k_0\sqrt{\rho^2+(R_a+2R_b)^2}\right)}{\left(\sqrt{\rho^2+(R_a+2R_b)^2}\right)^2}\left(k_0+\frac{1}{\sqrt{\rho^2+(R_a+2R_b)^2}}\right)\right] d\rho$$

$$= \frac{1}{2}\int_0^\infty \rho \left[\frac{R_a \exp\left(-k_0\sqrt{\rho^2+R_a^2}\right)}{\left(\sqrt{\rho^2+R_a^2}\right)^2}\left(k_0+\frac{1}{\sqrt{\rho^2+R_a^2}}\right) + \frac{(R_a+2R_b)\exp\left(-k_0\sqrt{\rho^2+(R_a+2R_b)^2}\right)}{\left(\sqrt{\rho^2+(R_a+2R_b)^2}\right)^2}\left(k_0+\frac{1}{\sqrt{\rho^2+(R_a+2R_b)^2}}\right)\right] d\rho$$

$$= \frac{1}{2}R_a\left[-\frac{\exp(-k_0\sqrt{\rho^2+R_a^2}}{\sqrt{\rho^2+R_a^2}}\right]_0^\infty + \frac{1}{2}(R_a+2R_b)\left[-\frac{\exp(-k_0\sqrt{\rho^2+(R_a+2R_b)^2}}{\sqrt{\rho^2+(R_a+2R_b)^2}}\right]_0^\infty$$

$$= \frac{1}{2}\left[\exp(-k_0R_a) + \exp(-k_0(R_a+2R_b))\right]$$

For determining the photons collected by fiber, radially dependent diffuse reflectance is integrating over the fiber diameter as

$$R_\rho(R_a) = \int_0^\rho R(\rho, R_a) 2\pi\rho d\rho$$

$$= \frac{1}{2}\int_0^d \rho \left[\frac{R_a \exp\left(-k_0\sqrt{\rho^2+R_a^2}\right)}{\left(\sqrt{\rho^2+R_a^2}\right)^2}\left(k_0+\frac{1}{\sqrt{\rho^2+R_a^2}}\right) + \frac{(R_a+2R_b)\exp\left(-k_0\sqrt{\rho^2+(R_a+2R_b)^2}\right)}{\left(\sqrt{\rho^2+(R_a+2R_b)^2}\right)^2}\left(k_0+\frac{1}{\sqrt{\rho^2+(R_a+2R_b)^2}}\right)\right] d\rho$$

$$= \frac{1}{2}\int_0^d \rho \left[\frac{R_a \exp\left(-k_0\sqrt{\rho^2+R_a^2}\right)}{\left(\sqrt{\rho^2+R_a^2}\right)^2}\left(k_0+\frac{1}{\sqrt{\rho^2+R_a^2}}\right) + \frac{(R_a+2R_b)\exp\left(-k_0\sqrt{\rho^2+(R_a+2R_b)^2}\right)}{\left(\sqrt{\rho^2+(R_a+2R_b)^2}\right)^2}\left(k_0+\frac{1}{\sqrt{\rho^2+(R_a+2R_b)^2}}\right)\right] d\rho$$

$$= \frac{1}{2} R_a \left[-\frac{\exp(-k_0\sqrt{\rho^2 + R_a^2})}{\sqrt{\rho^2 + R_a^2}} \right]_0^{\rho} + \frac{1}{2}(R_a + 2R_b) \left[-\frac{\exp(-k_0\sqrt{\rho^2 + (R_a + 2R_b)^2})}{\sqrt{\rho^2 + (R_a + 2R_b)^2}} \right]_0^{\rho}$$

$$= \frac{1}{2}\left[\exp(-k_0 R_a) + \exp(-k_0(R_a + 2R_b))\right] - \frac{1}{2}\left[\frac{R_a \exp(-k_0\sqrt{d^2 + {R_a}^2})}{\sqrt{d^2 + {R_a}^2}} + \frac{(R_a + 2R_b)\exp(-k_0\sqrt{d^2 + (R_a + 2R_b)^2})}{\sqrt{d^2 + (R_a + 2R_b)^2}} \right]$$

3.3 Relationship of scattering coefficient with Reflectance in semi-infinite medium

The diffuse reflectance R for a semi-infinite medium [80]

$$R = \frac{\alpha'}{1 + 2k(1 - \alpha') + \left(1 + \frac{2k}{3}\right)\sqrt{3(1 - \alpha')}} \tag{37}$$

$$\Rightarrow R\left\{1 + \frac{2k\,\mu_a}{\mu_a + \mu'_s} + \left(1 + \frac{2k}{3}\right)\sqrt{\frac{3\,\mu_a}{\mu_a + \mu'_s}}\right\} = \frac{\mu'_s}{\mu_a + \mu'_s}$$

$$\Rightarrow R\left\{\sqrt{\frac{\mu_a + \mu'_s}{\mu_a}} + 2k\sqrt{\frac{\mu_a}{\mu_a + \mu'_s}} + \left(1 + \frac{2k}{3}\right)\sqrt{3}\right\} = \frac{\mu'_s}{\sqrt{\mu_a(\mu_a + \mu'_s)}}$$

$$\Rightarrow R\left\{\frac{\mu_a + \mu'_s + 2k\,\mu_a}{\sqrt{\mu_a + \mu'_s}}\right\} - \frac{\mu'_s}{\sqrt{\mu_a + \mu'_s}} = -\left(1 + \frac{2k}{3}\right)\sqrt{3}\,\mu_a$$

If μ_a is very small, then $\sqrt{\mu_a + \mu'_s}$ can be written as $\sqrt{\mu'_s}$

$$\Rightarrow \frac{\mu'_s(R - 1) + R\,\mu_a(2k + 1)}{\sqrt{\mu'_s}} = -\left(1 + \frac{2k}{3}\right)\sqrt{3}\,\mu_a$$

$$\Rightarrow \mu'_s(R - 1) + \left(1 + \frac{2k}{3}\right)\sqrt{3}\,\mu_a\sqrt{\mu'_s} = -R\,\mu_a(2k + 1)$$

$$\Rightarrow \sqrt{\mu'_s}\left\{\sqrt{\mu'_s}(R - 1) + \left(1 + \frac{2k}{3}\right)\sqrt{3}\,\mu_a\right\} = -R\,\mu_a(2k + 1)$$

$$\Rightarrow \sqrt{\mu'_s}(R - 1) = -R\,\mu_a(2k + 1) - \left(1 + \frac{2k}{3}\right)\sqrt{3}\,\mu_a$$

$$\Rightarrow \mu'_s = \left\{ \frac{R\mu_a(2k+1)+\left(1+\frac{2k}{3}\right)\sqrt{3}\mu_a}{1-R} \right\}^2$$

3.4 Normalization Method

The materials that were used for reference include diffuse reflectance standards, 20% bulk intralipid, water & air. Intralipid, water and air, infinite medium geometry was applied whereas for the case of diffuse reflectance standard, we applied a semi-infinite medium geometry. Based on the geometry of references, the reflectance intensity model can be shown for intralipid, air and water as

$$I_{intralipid}(\lambda) = \frac{1}{2}\left[\exp(-k_0 R_a) - \frac{R_a \exp(-k_0\sqrt{d^2+{R_a}^2})}{\sqrt{d^2+{R_a}^2}}\right]_{intralipid} S(\lambda)+\eta_{fib/intralipid}S(\lambda)+\eta_{\text{int}}S(\lambda)$$

here $R_a = {}^{1}/_{\mu'_s}$ and reduced scattering coefficient for intralipid is derived by

$$\mu'_s = 127.0[c] - 205.3[c]^2 \tag{38}$$

where [c] is the concentration of intralipid [83]

$$I_{air}(\lambda) = \eta_{fib/air}S(\lambda)+\eta_{int}S(\lambda) \tag{39}$$

$$I_{water}(\lambda) = \eta_{fib/water}S(\lambda)+\eta_{int}S(\lambda) \tag{40}$$

Depending on the fiber probing in tissue, it can either have an infinite or semi-infinite medium geometry. Infinite geometry is applicable when the fiber is inserted interstitially into the tissue and the intensity can be shown as

$$I_{tissue}(\lambda)=\frac{1}{2}\left[\exp(-k_0R_a)-\frac{R_a\exp(-k_0\sqrt{d^2+R_a{}^2})}{\sqrt{d^2+R_a{}^2}}\right]_{tissue} S(\lambda)+\eta_{fib/tissue}S(\lambda)+\eta_{\text{int}}S(\lambda) \quad (41)$$

When the fiber is laced on the surface of the tissue, due to change in measurement condition, the measured intensity also changed to

$$I_{tissue}(\lambda)=\frac{1}{2}\left[\exp(-k_0R_a)+\exp(-k_0(R_a+2R_b))\right]-\frac{1}{2}\left[\frac{R_a\exp(-k_0\sqrt{d^2+R_a{}^2})}{\sqrt{d^2+R_a{}^2}}+\frac{(R_a+2R_b)\exp(-k_0\sqrt{d^2+(R_a+2R_b)^2})}{\sqrt{d^2+(R_a+2R_b)^2}}\right]_{tissue} S(\lambda)$$
$$+\eta_{fib/tissue}S(\lambda)+\eta_{\text{int}}S(\lambda)$$

Normalization using diffuse reflectance standards applies a semi-infinite medium geometry as fiber tip is placed in contact with the surface of the standards.

$$I_{standards}(\lambda)=\frac{1}{2}\left[\exp(-k_0R_a)+\exp(-k_0(R_a+2R_b))\right]-\frac{1}{2}\left[\frac{R_a\exp(-k_0\sqrt{d^2+R_a{}^2})}{\sqrt{d^2+R_a{}^2}}+\frac{(R_a+2R_b)\exp(-k_0\sqrt{d^2+(R_a+2R_b)^2})}{\sqrt{d^2+(R_a+2R_b)^2}}\right]_{standards} S(\lambda)$$
$$+\eta_{fib/standards}S(\lambda)+\eta_{int}S(\lambda)$$

3.4.1 Intralipid and water based normalization

The normalized intensity with respect to water and intralipid is

$$I(\lambda)=\frac{I_{tissue}(\lambda)-I_{water}(\lambda)}{I_{intralipid}(\lambda)-I_{water}(\lambda)}$$

$$I(\lambda)=\frac{\frac{1}{2}\left[\exp(-k_0R_a)-\frac{R_a\exp(-k_0\sqrt{d^2+R_a{}^2})}{\sqrt{d^2+R_a{}^2}}\right]_{tissue} S(\lambda)+\eta_{fib/tissue}S(\lambda)-\eta_{fib/water}S(\lambda)}{\frac{1}{2}\left[\exp(-k_0R_a)-\frac{R_a\exp(-k_0\sqrt{d^2+R_a{}^2})}{\sqrt{d^2+R_a{}^2}}\right]_{intralipid} S(\lambda)+\eta_{fib/intralipid}S(\lambda)-\eta_{fib/water}S(\lambda)}$$

$$= \frac{\left[\exp(-k_0 R_a) - \frac{R_a \exp(-k_0\sqrt{d^2 + {R_a}^2})}{\sqrt{d^2 + {R_a}^2}}\right]_{tissue}}{\left[\exp(-k_0 R_a) - \frac{R_a \exp(-k_0\sqrt{d^2 + {R_a}^2})}{\sqrt{d^2 + {R_a}^2}}\right]_{intralipid} + 2(\eta_{fib/intralipid} - \eta_{fib/water})}$$
$$+ \frac{2(\eta_{fib/tissue} - \eta_{fib/water})}{\left[\exp(-k_0 R_a) - \frac{R_a \exp(-k_0\sqrt{d^2 + {R_a}^2})}{\sqrt{d^2 + {R_a}^2}}\right]_{intralipid} + 2(\eta_{fib/intralipid} - \eta_{fib/water})}$$

3.4.2 Air and water based normalization

When normalized with respect to air and water, the normalized intensity becomes

$$I(\lambda) = \frac{I_{tissue}(\lambda) - I_{water}(\lambda)}{I_{air}(\lambda) - I_{water}(\lambda)}$$

$$I(\lambda) = \frac{\frac{1}{2}\left[\exp(-k_0 R_a) - \frac{R_a \exp(-k_0\sqrt{d^2 + {R_a}^2})}{\sqrt{d^2 + {R_a}^2}}\right]_{tissue} S(\lambda) + \eta_{fib/tissue} S(\lambda) - \eta_{fib/water} S(\lambda)}{\eta_{fib/air} S(\lambda) - \eta_{fib/water} S(\lambda)}$$

$$= \frac{\frac{1}{2}\left[\exp(-k_0 R_a) - \frac{R_a \exp(-k_0\sqrt{d^2 + {R_a}^2})}{\sqrt{d^2 + {R_a}^2}}\right]_{tissue}}{\eta_{fib/air} - \eta_{fib/water}} + \frac{\eta_{fib/tissue} - \eta_{fib/water}}{\eta_{fib/air} - \eta_{fib/water}}$$

3.4.3 Normalization with respect to reflectance standards and water

Normalization using reflectance standards as semi-infinite medium results

$$I(\lambda) = \frac{I_{tissue}(\lambda) - I_{water}(\lambda)}{I_{99\%}(\lambda) - I_{2\%}(\lambda)}$$

Here

$$I_{tissue}(\lambda) = \frac{1}{2}\left[\exp(-k_0 R_a)+\exp(-k_0(R_a+2R_b))\right]\frac{1}{2}\left[\frac{R_a\exp(-k_0\sqrt{d^2+R_a^2})}{\sqrt{d^2+R_a^2}}+\frac{(R_a+2R_b)\exp(-k_0\sqrt{d^2+(R_a+2R_b)^2})}{\sqrt{d^2+(R_a+2R_b)^2}}\right]_{tissue} S(\lambda)$$
$$+ \eta_{fib/tissue} S(\lambda) + \eta_{\text{int}} S(\lambda)$$

$$I_{99\%}(\lambda) = \frac{1}{2}\left[\exp(-k_0 R_a)+\exp(-k_0(R_a+2R_b))\right]\frac{1}{2}\left[\frac{R_a\exp(-k_0\sqrt{d^2+R_a^2})}{\sqrt{d^2+R_a^2}}+\frac{(R_a+2R_b)\exp(-k_0\sqrt{d^2+(R_a+2R_b)^2})}{\sqrt{d^2+(R_a+2R_b)^2}}\right]_{99\%} S(\lambda)$$
$$+ \eta_{fib/99\%} S(\lambda) + \eta_{\text{int}} S(\lambda)$$

$$I_{2\%}(\lambda) = \frac{1}{2}\left[\exp(-k_0 R_a)+\exp(-k_0(R_a+2R_b))\right]\frac{1}{2}\left[\frac{R_a\exp(-k_0\sqrt{d^2+R_a^2})}{\sqrt{d^2+R_a^2}}+\frac{(R_a+2R_b)\exp(-k_0\sqrt{d^2+(R_a+2R_b)^2})}{\sqrt{d^2+(R_a+2R_b)^2}}\right]_{2\%} S(\lambda)$$
$$+ \eta_{fib/2\%} S(\lambda) + \eta_{\text{int}} S(\lambda)$$

And

$$I_{water}(\lambda) = \eta_{fib/water} S(\lambda) + \eta_{\text{int}} S(\lambda)$$

3.5 Mathematical characterization of normalized reflectance intensity and dependency on scattering properties

3.5.1 Model comparison with MC simulation

In this study, normalization techniques obtained by analytical model were compared with MC simulation. To compare the model performance with Monte Carlo studies done previously [3], all three normalization methods were applied in the same figure and results are shown in fig 3.3 (a). Figure 3.3 (b) shows the mathematical results for analytical modeling of normalized reflectance intensity against dimensionless scattering $(\mu'_s d)$ where μ'_s varied over a wide range [0.06-10000]

mm^{-1} and fiber diameter was 320µm. Here, reflectance intensity measured from the tissue surface is normalized with respect to air and water, intralipid and water and reflectance standards and water. The results show a similar pattern of regime transition when $\mu'_s d > 10$, irrespective of the reference medium condition used for the normalization purpose.

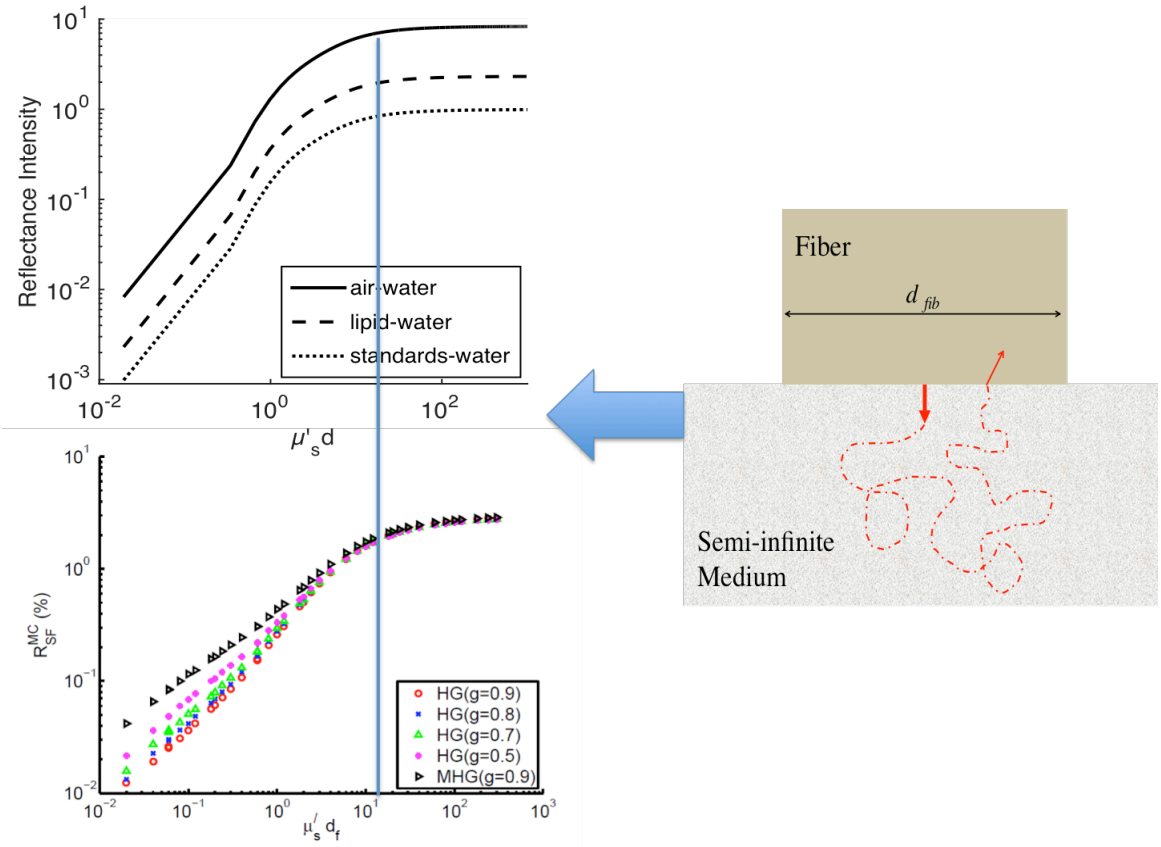

Figure 3.3: (a) Normalization of semi-infinite probing using different references obtained from analytical model. (b) Results from MC simulation for single fiber reflectance vs dimensionless scattering.

One of the limitations in previous MC simulations is that the tissue-probing condition was not considered there. Measurements from surface probing of the tissue were normalized with respect to semi-infinite references only. Here, for the sake of comparison, all normalizations were performed for surface measurement of tissue. The model agrees with MC simulation, especially when surface probing is normalized with respect to semi-infinite references.

3.5.2 Influence of fiber probing in tissue normalization

Fig 3.4, 3.5 and 3.6 shows the normalized intensity obtained from the model when both correct and wrong references are applied to different tissue probing. Interstitial and surface probing of tissue is normalized with air and water 3.4, intralipid and water 3.5 and with standards and water 3.6. From the figures 3.4-3.6, it can be investigated that, interstitial probing normalized with infinite medium and surface probing normalized with semi-infinite medium references shows a correct trend as seen from MC study. At the other hand, when semi-infinite references were applied to interstitial probing of tissue the plateau was reached before than normalized with infinite references which seems not to agree with theory.

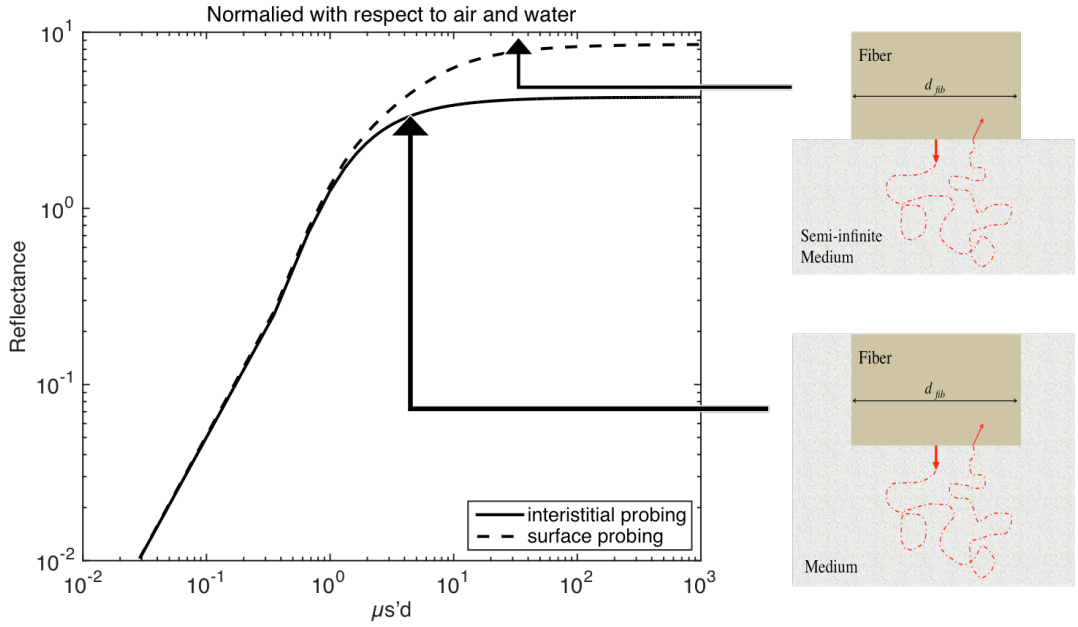

Figure 3.4: Reflectance vs dimensionless scattering for interstitial and surface probing normalized with respect to air and water.

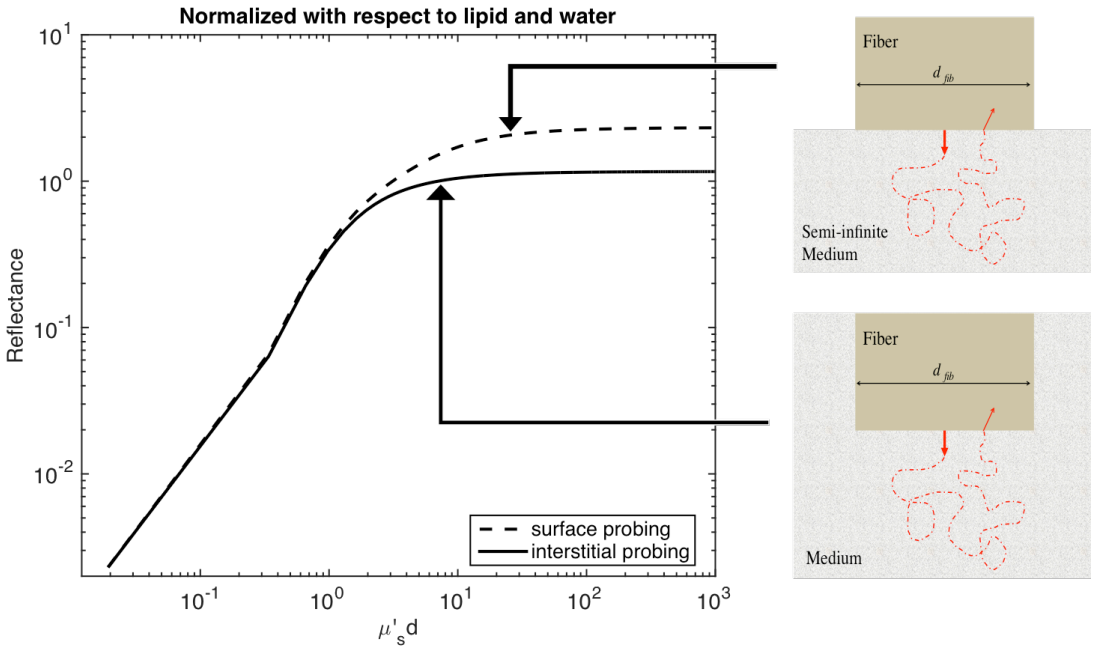

Figure 3.5: Reflectance vs dimensionless scattering for interstitial and surface probing normalized with respect to 20% intralipid and water.

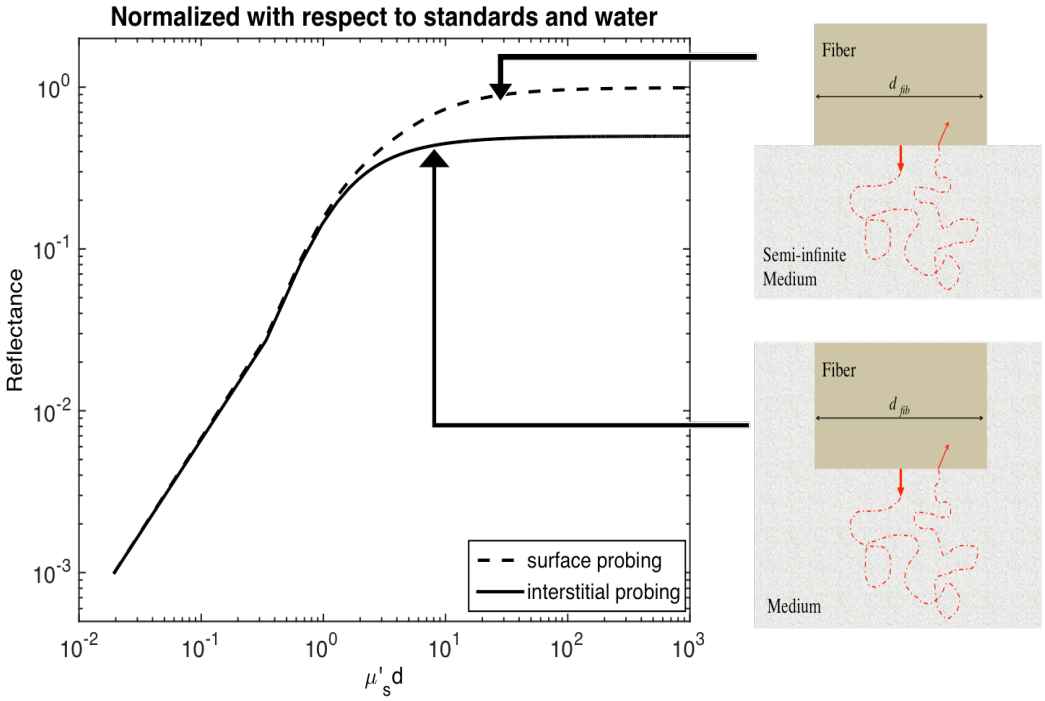

Figure 3.6: Reflectance vs dimensionless scattering for interstitial and surface probing normalized with respect to reflectance standards (99% and 2%) and water.

To understand more clearly what happened when the fiber was inserted into the tissue, three normalization techniques were applied considering respective probing geometry condition. Based from the analytical model, air-water and lipid-water based normalization was applied to interstitial probing of tissue measurements with the references representing infinite medium. The transition regime occurred after $\mu'_s d > 1$ for infinite medium cases, whereas for semi-infinite medium, reflectance intensity reached its plateau when $\mu'_s d > 10$. Surface measurement of tissue was normalized with respect to water and diffuse reflectance of high and low reflectivity. Thus the mathematical result of analytical modeling agreed with the theory of infinite and semi-infinite medium geometry.

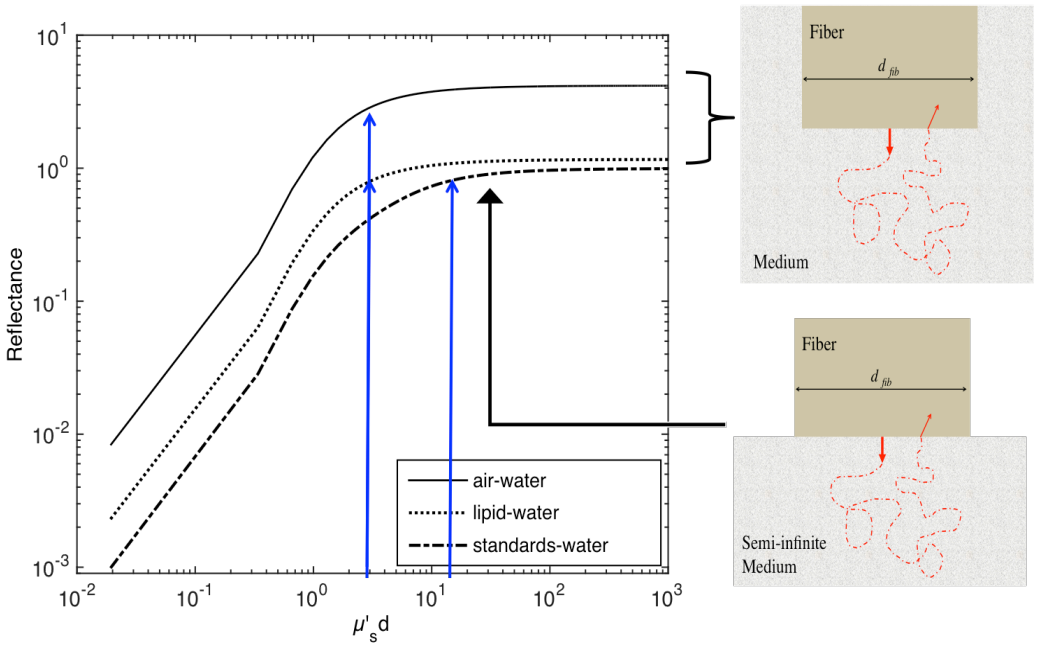

Figure 3.7: Reflectance vs dimensionless scattering from applying medium matched references for normalization.

3.6 Validation of MC using liquid optical phantom

The normalized SfRS measurement with variation in scattering properties of the medium is

further experimented using an intralipid solution as a liquid optical phantom. For a very lower range of scattering coefficient μ'_s ([0.02-1.2] mm^{-1}), different methods including air-water, lipid-water and standards-water based normalization were applied and normalized intensity at a single wavelength (632.8 nm) is plotted against μ'_s (fig 3.8). Here infinite medium references were considered as normalizing references for interistital probing and standards water combination used for surface probing. When the fiber probe is inserted into the intralipid solution it acts as an infinite medium, thus air-water and lipid-water based normalization is expected to be more accurate than reflectance standards-water based normalization.

3.6.1 Intralipid phantom preparation

The principle to quantitatively relate the normalized SfRS measurement with scattering properties of the medium was tested using intralipid solution as a very low absorbing liquid phantom by varying its scattering coefficient gradually. The liquid phantom was prepared by syringing 0.5ml of 20% bulk intralipid solution in a bottle containing 500ml of water. After injecting 0.5ml of 20% intralipid in the bottle, the bottle was shaken vigorously to ensure the proper mixing of the solution, and then SfRS measurement was performed in a dark room condition by placing the fiber probe in the middle of the solution. To maintain reasonably consistent SfRS measurement when operating in a darkroom, the probe fiber was housed in a rigid tube with a manual positioning mechanism to the liquid phantom in a plastic bottle.

A total of 50 repeated SfRS measurements were performed by adding 0.5ml 20% bulk intralipid at each round. Denote n as the round of adding the 0.5ml 20% bulk intralipid, n = [1, 50], then the volume concentration of the intralipid in the plastic bottle was $[C]_n = (0.5n \times 0.2)/[500 + 0.5n]$

The reduced scattering coefficient (unit: mm^{-1}) of the intralipid solution at each round of added 0.5ml 20% bulk intralipid was estimated by using the formula [20]

$$[\mu_s']_n \approx 127.0[C]_n - 205.3[C]_n^2$$

The SfRS measurement at the n-th round of added the 0.5ml 20% bulk intralipid to the bottled solution was normalized and at 632.8 nm the normalized intensity was extracted.

3.6.2 Normalization of liquid phantom

Normalization of prepared intralipid solution was performed at 632.8 nm using references from both infinite and semi-infinite medium geometry for the purpose of comparison.

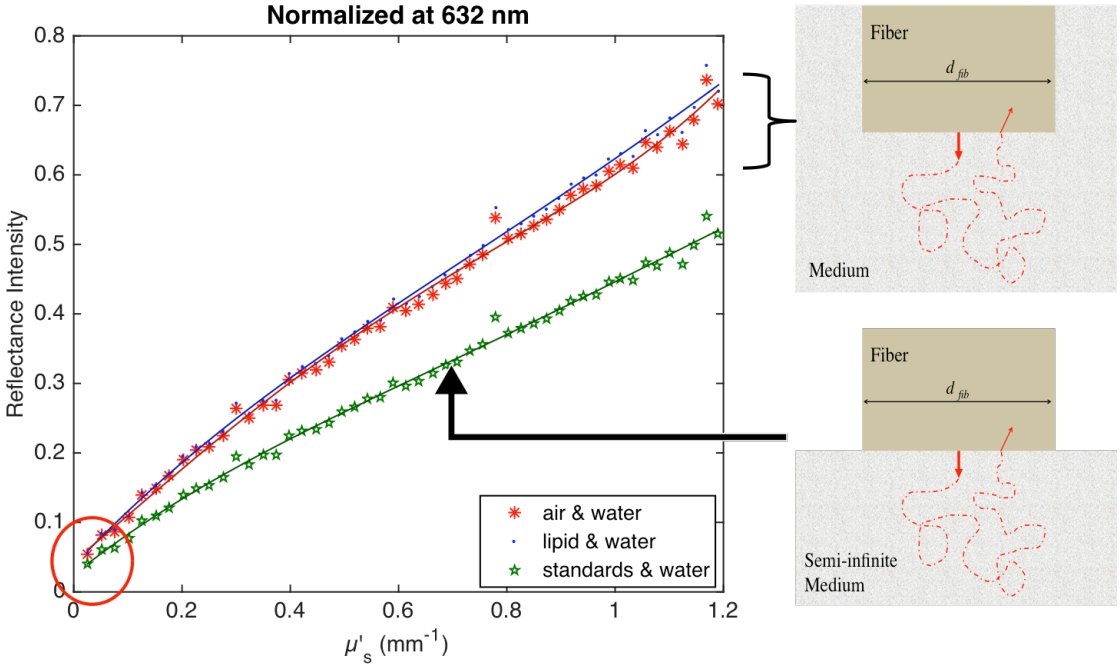

Figure 3.8: Reflectance intensity vs scattering coefficient at 632nm from air-water, intralipid-water and reflectance standards-water based normalization.

From figure 3.8, it can be seen that both air-water and inralipid water based normalization performing close to each other. Standards-water based semi-infinite normalization technique shows a smaller intensity level, which agrees with the theory due to taking account of contribution from real and image source. Here air and water based normalization technique is used for rat study as all the measurements were taken by percutaneous needle placement.

CHAPTER IV

MATERIALS AND METHODS

4.1 Diet and animal protocol

The animal protocol of this study was approved by the Institutional Animal Care and Use Committee of Oklahoma State University (protocol # VM-11-20). Twelve male Sprague-Dawley rats weighing 250-280 grams (Harlan Labs, Inc. Madison, WI) were housed individually in the university's Lab Animal Resources facility, and allowed food (control or test diet) and water *ad libitum*. All rats were acclimatized to laboratory conditions for a minimum of seven days and fed a standard rodent chow *ad libitum* (Laboratory Rodent Diet 5001, LabDiet, St. Louis, MO). The twelve rats were then randomly grouped to 4 control rats and 8 test rats. The control rats were fed an amino acid control diet *ad libitum* (Harlan Telkad – TD.130936), and the test rats were fed a methionine-choline-deficient (MCD) diet (Harlan Telkad – TD.90262) *ad libitum*. Percutaneous SfRS measurements of the rat livers were performed on day-0, day-13, day-27 day-41, and day-55 under trans-abdominal ultrasound guidance and respiration gated data acquisition. The identifications of the rats were blinded to the SfRS operators. At each of the days of 13, 27, 41, and 55, one control rat and two test rats were euthanized after their respective SfRS measurements and necropsied for gross examination and hepatic histology. At the completion of the *in vivo* studies he identities of the rats were reaveled for SfRS operations to compare the post-processed SfRS results with the histopathologic findings.

The experimental procedures for percutaneous SfRS of the rat liver are illustrated in Fig.4.1. At the time of examination, the rat was anesthetized using intraperitoneal administration (0.1 ml/100 g body weight) of a "cocktail" of xylazine (1.5 ml of 100 mg/ml) / ketamine (10 ml of 100 mg/ml) and preemptive analgesic subcutaneous dose of 0.1 ml per 100g body weight of buprenorphine (buprenorphine diluted 1:5 with sterile saline). This anesthetic regime was supplemented with oxygen and isofluorane as necessary via a facemask. The rat was placed in a dorsoventral position on an in-house U-shaped foam-bed. A pneumatic pillow sensor (SA Instruments, Stoney Brook, NY) was inserted under the caudal and left-lateral aspect of the thoracic area of the rat for respiration gating of the SfRS data acquisition. The ventral abdomen extending cranial from the brim of the pelvis to the xyphoid was clipped of hair and surgically prepped with an antiseptic solution (chlorhexidine scrub – Vetco, St. Joseph, MO). Using ultrasound guidance (Aloka Prosound Alpha 6 console and 9120 transducer at 8MHz, sectional field-of-view of radius 3.5cm, gain setting of 75, and contrast setting of 10), a sterile, 20-gauge 1.5-inch myelographic needle was inserted through the skin, abdominal musculature, and peritoneum into the liver. The guide needle was placed within the iver parenchyma in areas void of apparent vasculature in the vicinity of the needle tip as evaluated by gray scale ultrasound and crosschecked by Doppler ultrasound when needed. The ultrasound probe was held in position using an adaptable tripod with a cable holder to maintain continuous stabilized visualization of the needle within the intra-parenchyma field during SfRS measurements.

After retracting the needle's stylet of the needle, a sterile 320μm single-fiber probe (low-OH quartz fiber, H320R, New Star Lasers, Roseville, CA, standard for use with percutaneous laser disc ablation and lithotripsy) was inserted through the needle lumen. Prior to placing the fiber-probe in the needle, reference measurements from air and water for normalizing the SfRS readings from tissue were taken. The placing of the fiber-probe in the needle was monitored by

ultrasound till the fiber tip extruded the beveled needle tip a few millimeters, as indicated by the arrows on the photograph in Fig. 4.1.

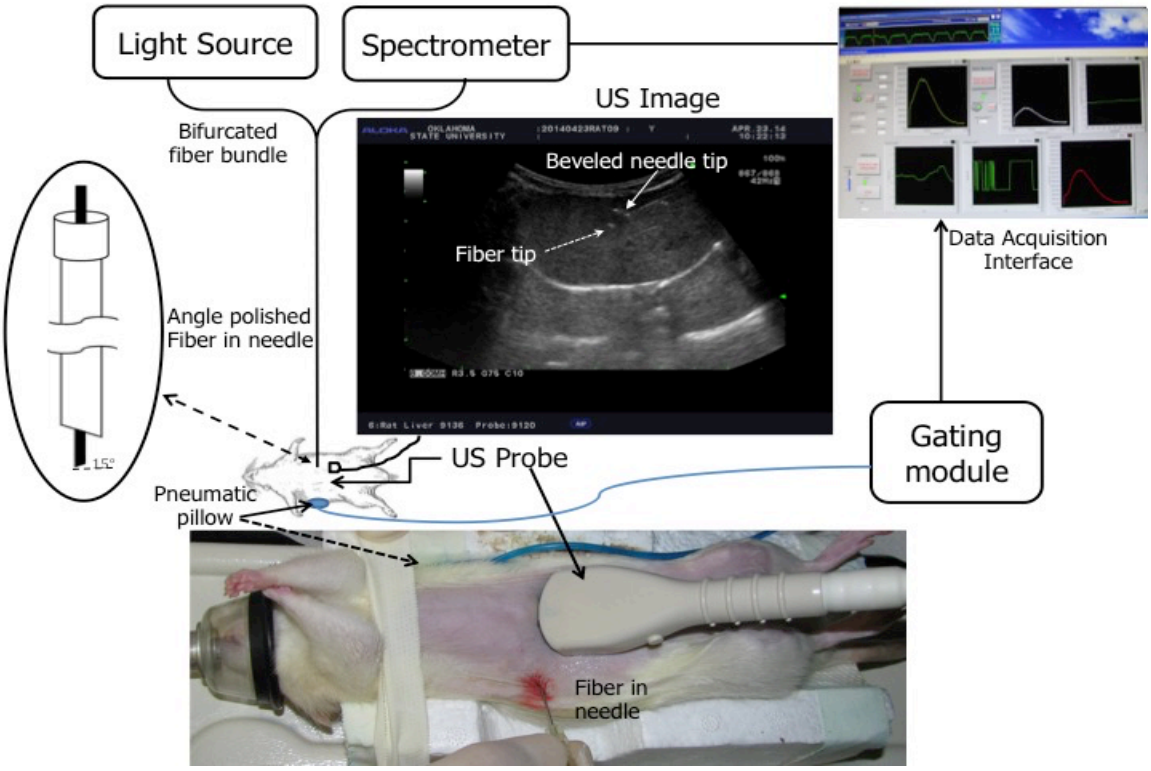

Figure 4.1: The configuration for percutaneous SfRS of rat liver. Light source and spectrometer were coupled to a 200μm bifurcated fiber bundle (shown at top-left) to which a 320μm single fiber probe was connected. The single fiber probed into liver through a 20 gauge needle (schematic of angle polished fiber in needle shown at left), by ultrasound guidance (see the photograph in the middle panel). From the pneumatic pillow (covered by the rat and the small air tubing shadowed by the ultrasound cable), respiration of the rat was detected by a gating module for triggering the SfRS data acquisition (the triggering sequence is shown at the top right).

Five repeated measurements, each with a 100ms time of integration of the signal after triggered by the respiration gating output, were acquired from each subject. In the off-line processing, the five SfRS measurements were averaged for subsequent spectral analysis as detailed in the following section of "Method of SfRS analysis". After the percutaneous SfRS measurements, the rats to remain in the study were revived and returned to their cages for observation, and the rats to

be euthanized underwent a midline ventral incision extending cranially through the xyphoid and diaphragmatic reflection into the chest cavity using a #10 scalpel blade. A 20-gauge needle with a 3 cc syringe was then used to collect approximately 2 cc of whole blood by direct intracardiac puncture for laboratory analysis. Immediately following blood collection, a direct intracardiac injection of 1 cc (390 mg) of pentobarbital sodium (Beuthansia D, Schering Plough, Union, NJ) was administered to induce euthanasia. Necropsy was performed immediately, followed by fixing the specimens of livers in 10% buffered formalin. The liver specimens were trimmed in and keyed. When sections were returned, the pathologist examined under routine hematoxylin / eosin (H&E) staining and the microscopy images (for lipid determination) blinded to the groups and ranked the sections in order based upon amount of lipid accumulation. After ranking as reported in the "Results" section, the animal identification was obtained by checking the section number with the key.

4.2 SfRS System Configuration

4.2.1 Single fiber configuration for needle based probing of tissue

Figure 4.2 shows the schematic of Single fiber Reflectance spectroscopy system setup. The experimental setup consisted of a halogen deuterium light source (DH2000-FHS, Ocean Optics, Dunedin, FL), a spectrometer (USB 4000-VIS-NIR, Ocean Optics, Netherlands) and a single optical fiber. The light source and spectrometer were connected through a bifurcated fiber bundle (BIF 200-VIS/NIR, Ocean Optics, Inc.) and the combined end of bifurcated fiber was connected to 320μm diameter single fiber. The single optical fiber used for both delivering light to the measurement medium and collecting light remitted from that medium. Photons coming from light source travel through the fiber and entered into the medium that was in contact with the fiber tip. The backscattered photons with an incident angle, which was within the numerical aperture of the

fiber core was moved back to the spectrometer. The probe tip was polished at an angle of 15^0 to remove specular reflection at the fiber tip due to reflectance index mismatch at the fiber to medium interface [84]. To insert the fiber into the tissue for percutaneous measurements, a 20-gauge 1.5-inch myelographic needle was used through which the fiber tip was placed into the liver parenchyma.

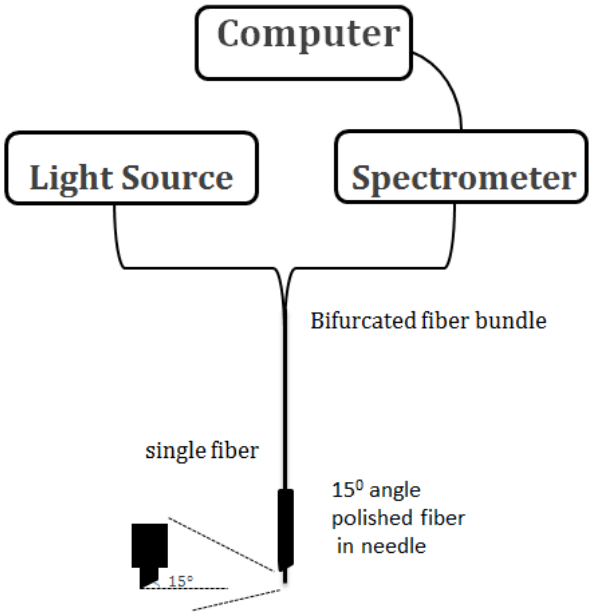

Figure 4.2: Schematic of Single fiber reflectance spectroscopy experimental setup.

4.2.2 SfRS data acquisition and respiration gating implementation

To collect the reflectance spectrum from rat liver, the 320μm single optical fiber was inserted through the 20-gauge needle and then introduced percutaneously in the rat liver while needle positioning was guided via ultrasound. A respiration gating system was implemented with controllable threshold to start SfRS data acquisition for maintaining data consistency and minimizing fluctuation in signal due to respiratory movements. The respiration gating system consisted of a pneumatic pillow and a small animal monitoring & gating module (Model 1025T,

SA Instruments, Inc. Stony Brook, NY). The pneumatic pillow was placed in contact with the dorsolateral aspect of the thorax of the rat to detect breathing induced movements and the gating signal was monitored in a graphical user interface (GUI). Adjusting the breathing threshold for of each rat, all the SfRS data was collected. The computer interfaced GUI including the SfRS measurement panel, were incorporated in LABVIEW (National Instruments, Austin, TX). During SfRS measurements, GUI audiblizeed different audible sounds that were preset for the respiration gating condition as well as starting of data acquisition (Fig 4.3).

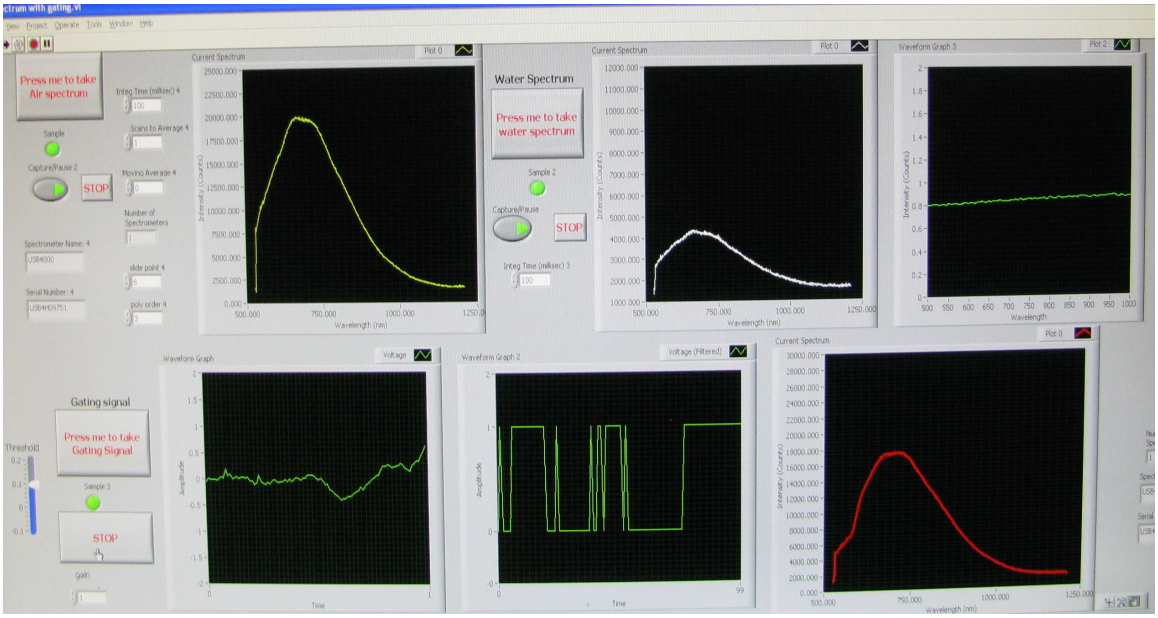

Figure 4.3: Data acquisition interface. Air and water spectrum on first row, along with audio files plays upon starting the button to start taking spectrum. The adjustable threshold (blue slide swich on left side of rw two) used to generate Schmitt trigger depending on breathing signal (first image in row two) from respiration gating module and the SfR spectrum from sample liver (right corner of row two). Air and water based normalization of sample tissue shown at right side of first row.

The sound intensity level varied depending on the SfRS intensity of samples that were being measured. The experiments were conducted in three steps. First, all 12 rats were anesthetized and the fiber was placed percutaneously in the rat liver parenchyma as guided by ultrasound to assess

the SfRS spectrum. Five sets of data were collected from each rat. Next, the livers of two test rats and one control rat were exposed via midline laparotomy and five sets of SfRS data were collected from each of the three lobes of rat liver by performing both surface and interstitial probing of the fiber. At the time of last step, the three laparotomized rats were euthanized and again five sets of antimortem measurements were taken again immediately postmortem from each lobe. All measurements were performed in a darkened room condition. Experiments were performed at 14 days intervals.

CHAPTER V

RESULTS

5.1 Histological evaluation and steatosis grading

The four control rats euthanized at day 12, day 27, day 41 and day 55 did not exhibit steatosis and were classified within the insignificant steatosis accumulation group. The mild steatosis group consisted of three test rats, two euthanized at day 13 and one at day 27. The moderate steatosis group contained one test rat, which was euthanized at day 27. Finally, the severe steatotis group consisted of four test rats, two euthanized at day 41 and the remaining two sacrificed at day 55. The degree of steatosis in control and test rats is presented in table 1, according to their day of euthanasia. The comparative microscopic images are presented in figure 5.1.

Group	**Insignificant**	**Mild**	**Moderate**	**Severe**
Type	Control# 4	Test# 3	Test# 1	Test# 4
Euthanized at day	13, 27, 41, 55	13, 13, 27	27	41, 41, 55, 55

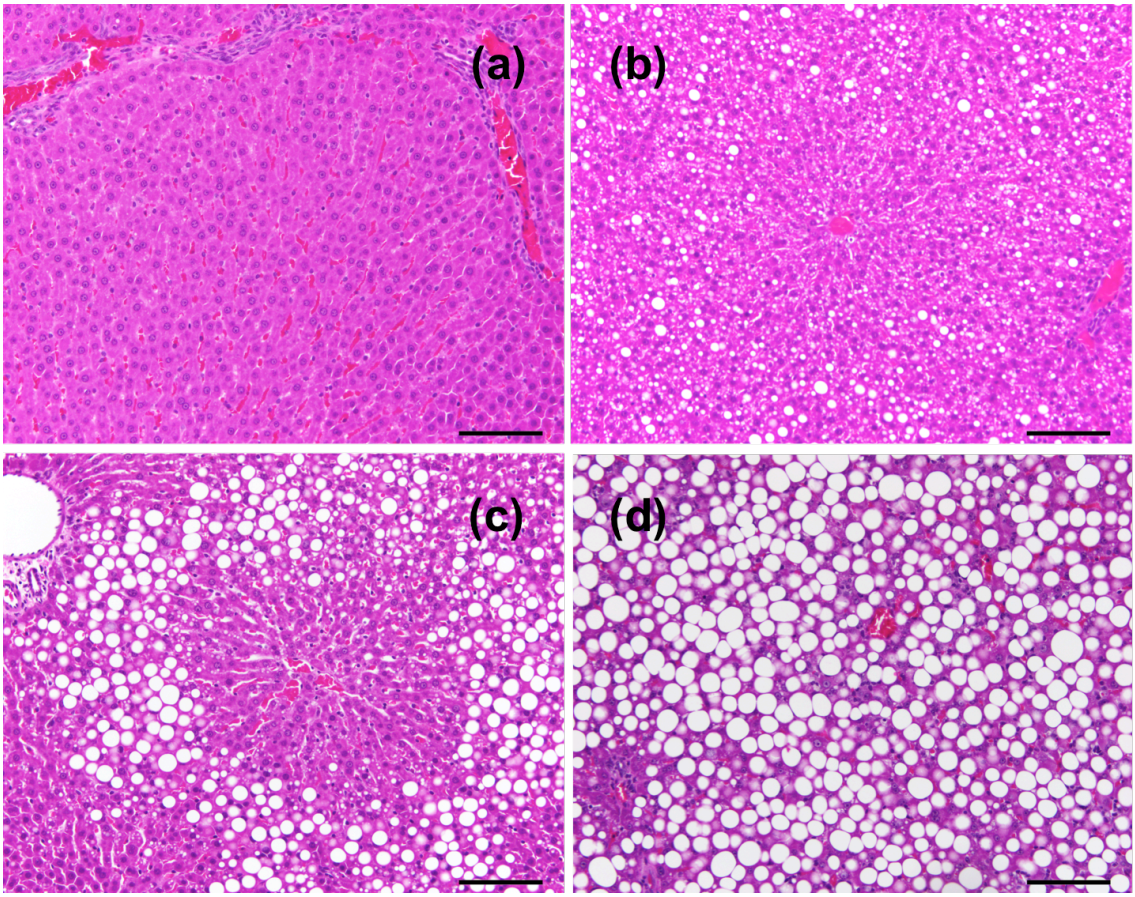

Figure 5.1: Photomicrograph of euthanized rats having (a) insignificant lipid accumulation, (b) mild lipid accumulation, (c) moderate lipid accumulation and (d) severe lipid accumulation.

5.2 SfRS measurements performed on baseline and the day of euthanasia

The changes of the SfRS measurements $I_{norm}(\lambda)$ of the 12 rats from the baseline to their respective days of euthanasia are presented in Fig. 5.2, according to the individual group of rats based on day of euthanasia. The $I_{norm}(\lambda)$ of the rat originating from the control group is plotted as a solid black line, and the measurements of the two rats of the test group are plotted as respectively as the dotted and dashed lines. Out of the 3 rats euthanized on day 13, the one control rat had insignificant lipid accumulation in the liver, and both of the two test rats had mild lipid accumulation. Out of the 3 rats euthanized on day 27, the one control rat had insignificant lipid

accumulation in the liver, one test rat (dotted blue line) had mild lipid accumulation and the other test rat (dashed red line) had moderate lipid accumulation. Out of the 3 rats euthanized on day 41, the one control rat had insignificant lipid accumulation in the liver; other two test rats (dotted blue line and dashed red line) had severe lipid accumulation. Finally, out of the 3 rats euthanized on day 55, the one control rat had insignificant lipid accumulation in the liver, and two test rats (dotted blue line and dashed red line) had severe lipid accumulation.

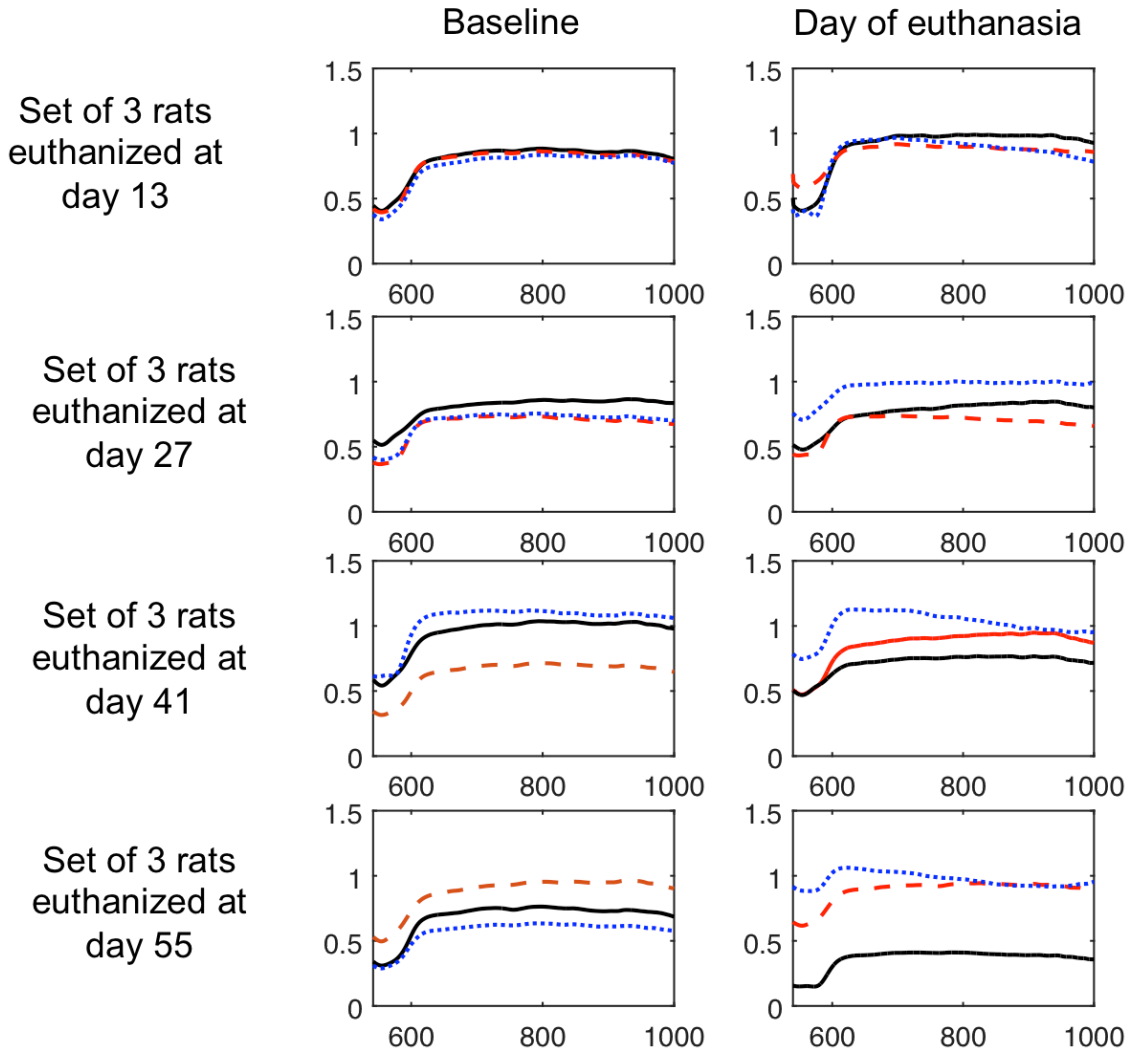

Figure 5.2: Comparison of the normalized SfRS measurements $R_{norm}(\lambda)$ from the baseline (left panel) to the respective days of euthanasia (right panel). The measurement from the rat originated from the control group is plotted as a solid black line. The measurements from the two rats in the test group are plotted as respectively dotted and dashed lines.

5.3 Scattering profile extraction

5.3.1 Scattering profile based on SfRS measurements

The procedure of extracting scattering profile out of SfRS raw spectrum is shown in Fig 5.3. Firstly, raw spectrum is normalized with respect to air and water in order to decouple the source spectral profile and internal reflection from fiber along with collection efficiency. The normalized

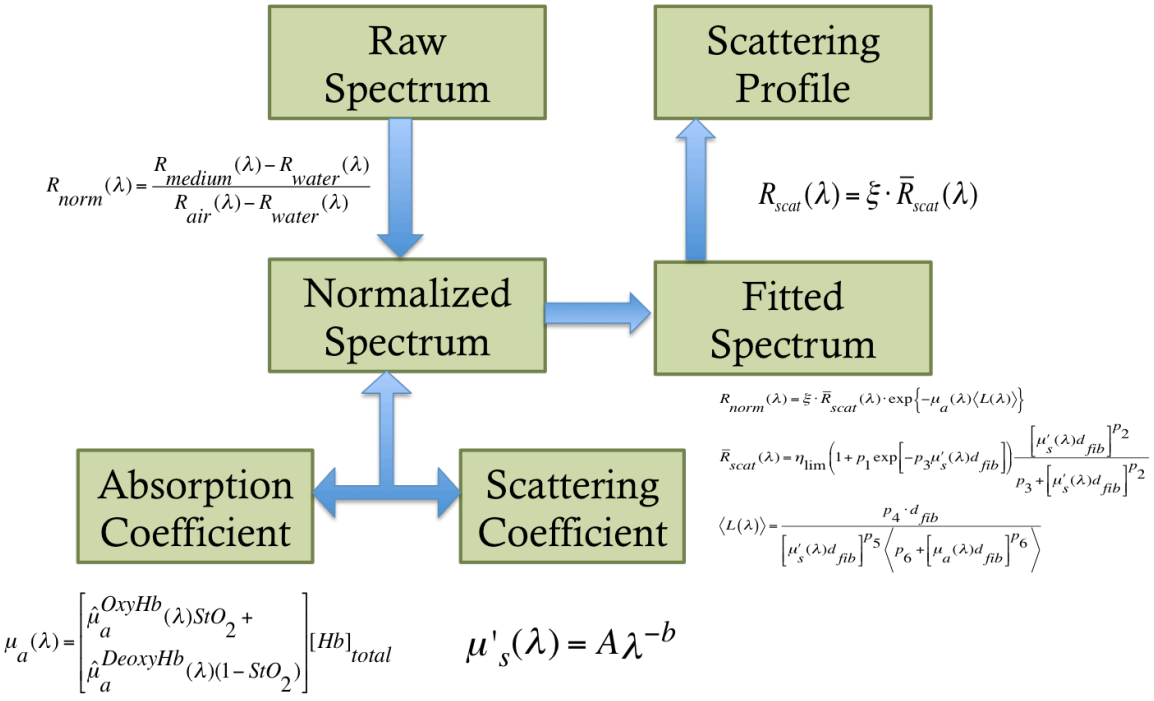

Figure 5.3: Steps to extract scattering profile from SfRS spectrum from rat liver.

spectrum now shows the tissue optical properties, basically the absorption and scattering of light by tissue particles. While absorption occurs at lower wavelength range due to presence of oxyhemoglobin and deoxyhemoglobin; the scattering occurs at the higher wavelength region. The scattering profile depends on a reduced scattering coefficient, which changes due to change in a number of factors such as particle number density, size distribution, average particle size etc.

Using equation [2], $R_{norm}(\lambda) = \xi \cdot \bar{R}_{scat}(\lambda) \cdot \exp\left\{-\mu_a(\lambda)\langle L(\lambda)\rangle\right\}$ normalized spectrum is fitted with fitting parameters and the absorption portion is then decoupled from the simulated normalized curve to get only the contribution from scattering (Fig 5.4).

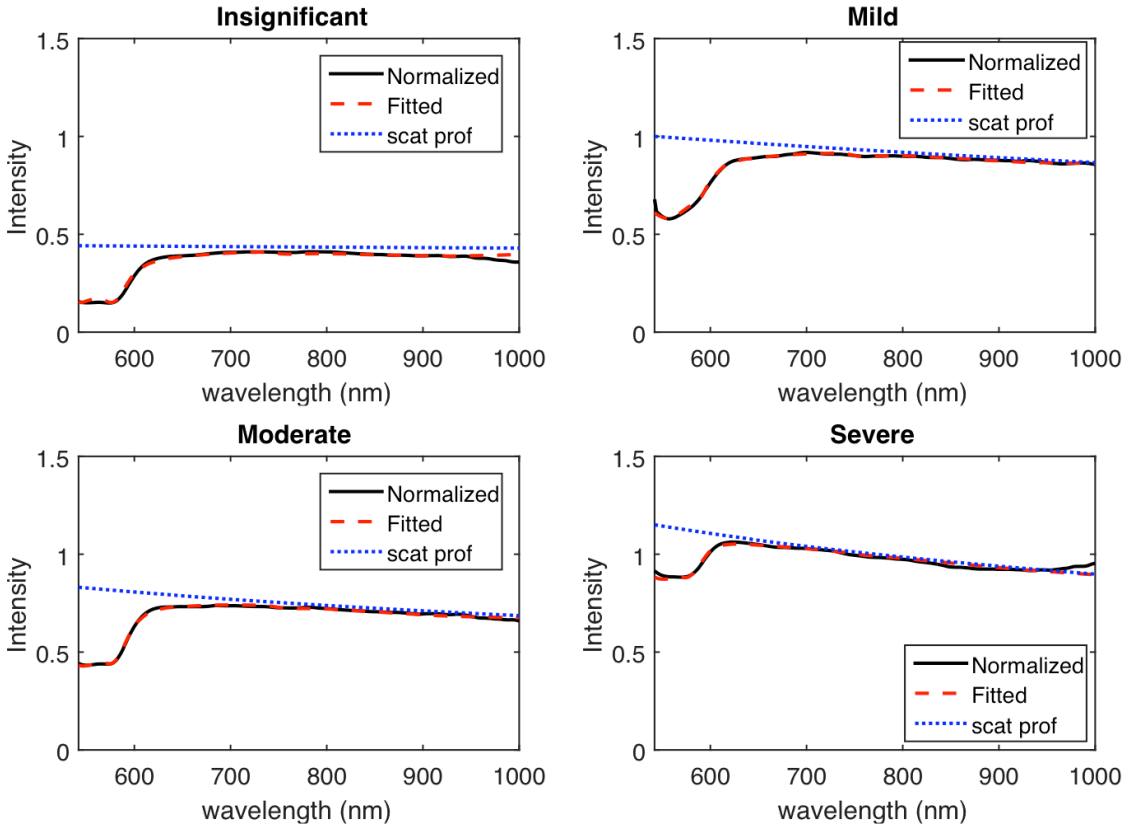

Figure 5.4: Normalized SfRS spectrum with respect to air and water (black solid line), fitted spectrum using equation to fit $R_{norm}(\lambda)$ (red dashed line) and scattering profile obtained from decoupling absorption out from $R_{norm}(\lambda)$ (blue dotted line) for (a) insignificant lipid accumulation, (b) mild, (c) moderate and (d) severe lipid accumulation.

5.3.2 Scattering profile base on histopathology image analysis

The microscopy images of all twelve rats used for this test study contain information about size distribution of lipid particle and their average size with number density which can further be used

to get scattering information of each rat depending on their lipid accumulation. The process is described in Fig 5.5.

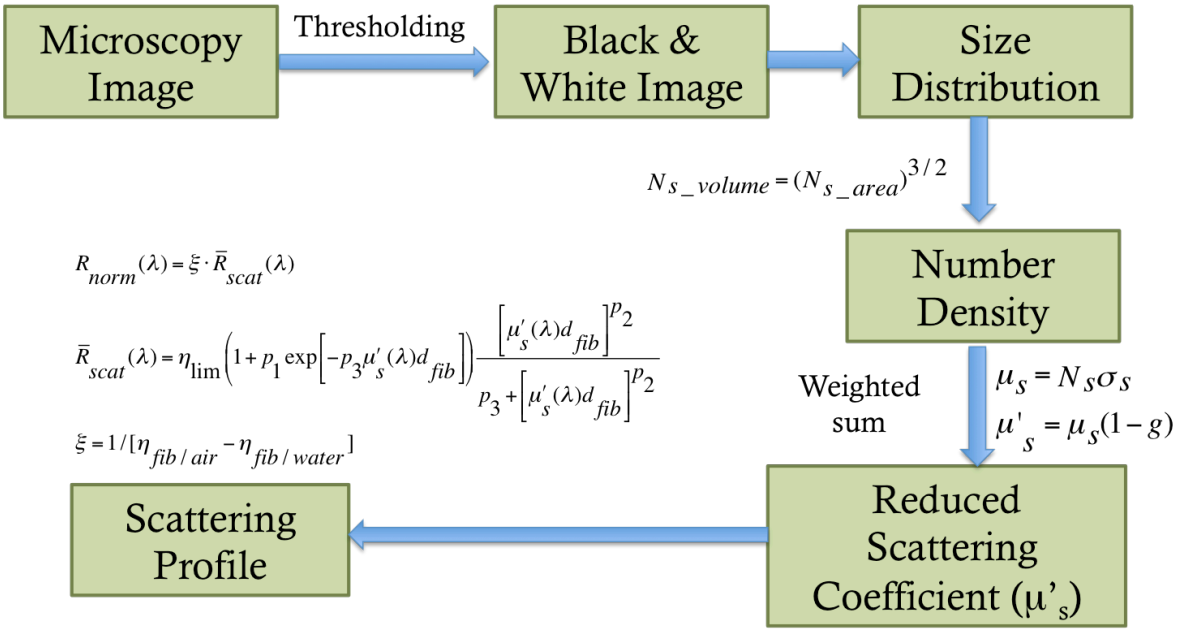

Figure 5.5: Steps to extract scattering profile from histology image.

To convert a photomicrograph into a black and white image, a threshold of 0.85 is used so that all particles with even smaller sizes also exist in image (Fig 5.6).

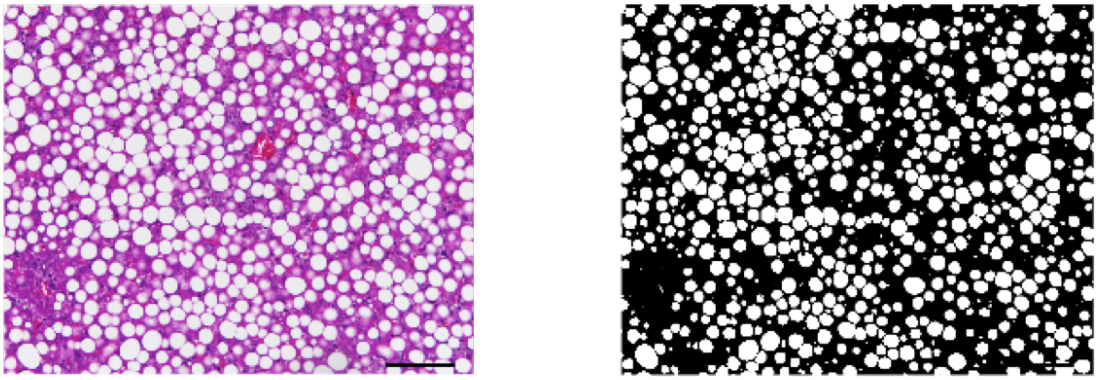

Fig 5.6: (a) Photomicrograph and (b) binary image with threshold 0.85.

The binary images were analyzed to get the scattering profile from each rat liver. The scattering profile of the normalized spectrum is mainly due to the scattering coefficient of tissue, which contains information about particle number density in volume and a scattering cross section.

To assess the particle number density in volume, the equivalent diameter of each particle and associated number counted for each image with different grade of lipid accumulation (Fig 5.7).

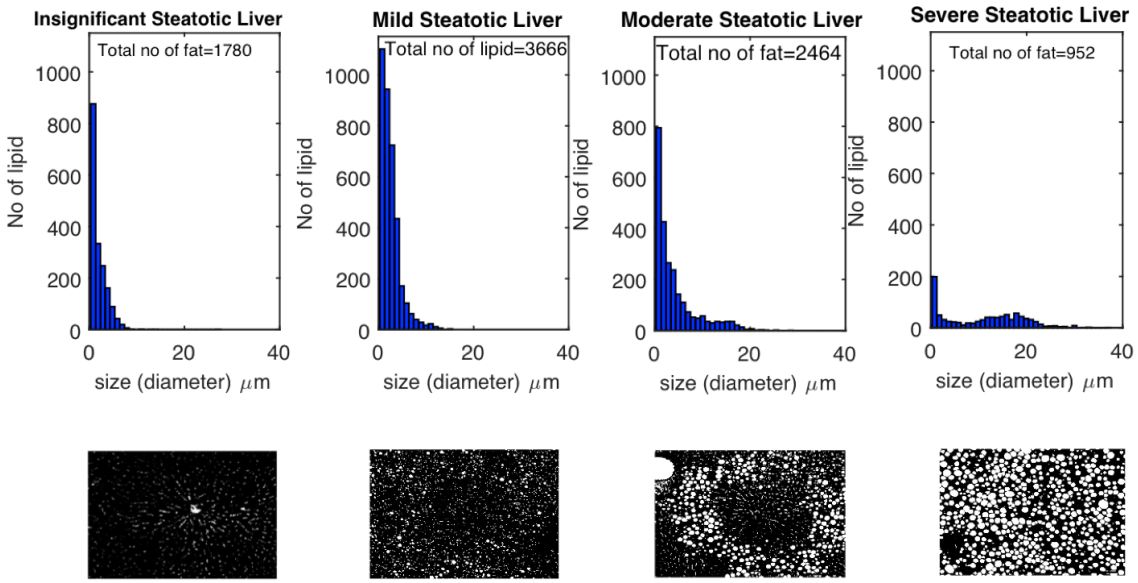

Figure 5.7: Size distribution of lipid vacuoles from binary image, (a) insignificant steatotic liver, (b) mild, (c) moderate and (d) severe steatotic liver.

As, the binary images are in 2-dimensions, analyzing the images for particle number density in area is calculated first. The number density of scattering particle in volume is then calculated from number density in area as [87]:

$$N_{s\_volume} = (N_{s\_area})^{3/2}$$

The reduced scattering coefficient could be calculated by

$$\mu_s(\lambda) = N_{s\_volume}\sigma_s$$

$$\mu'_s(\lambda) = \mu_s(\lambda)(1 - g(\lambda))$$

The scattering profile is extracted using images showing similar trends like the scattering profile observed from SfRS measurement analysis. The black solid line represents the normalized spectrum and the red dotted line represents the fitted spectrum using the equation [2]. To get tissue scattering information only, the absorption part is removed from the fitted curve where the required μ'_s is used in analyzing the image (Figure 5.8).

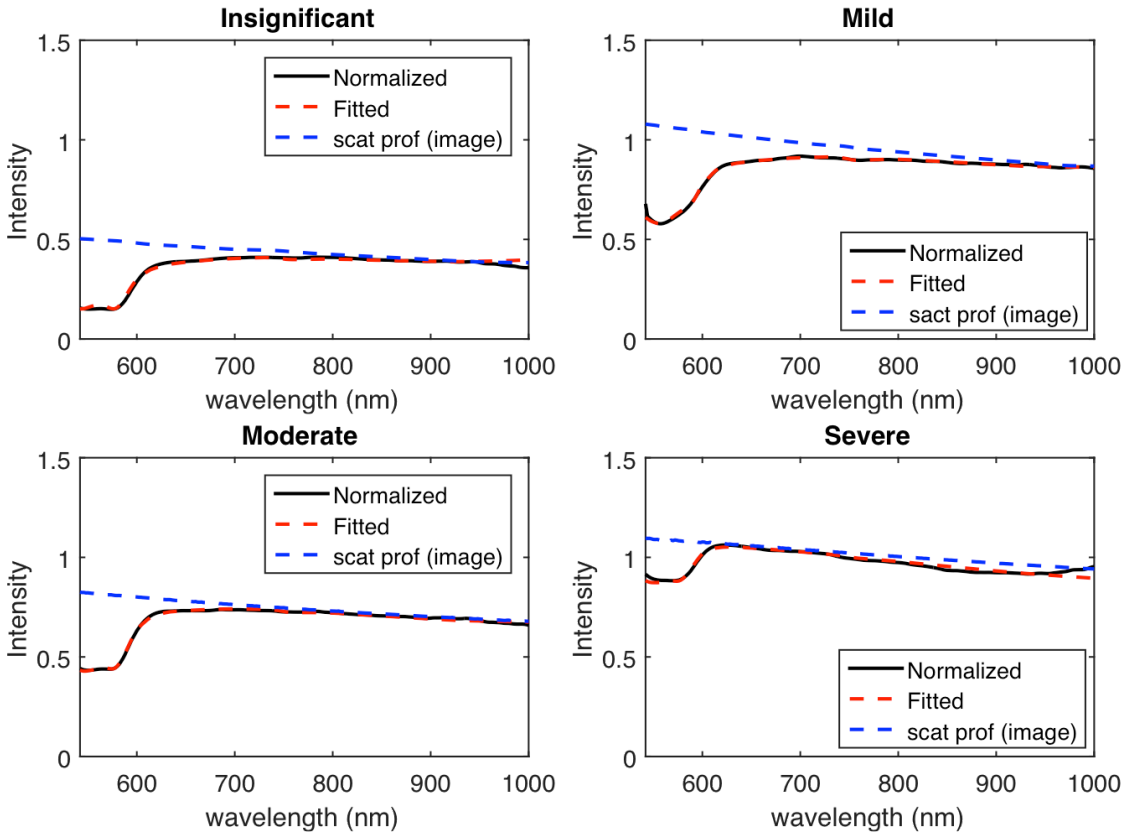

Figure 5.8: The ormalized SfRS spectrum with respect to air and water (black solid line), fitted spectrum using equation to fit $R_{norm}(\lambda)$ (red dashed line) and scattering profile obtained from decoupling absorption out from $R_{norm}(\lambda)$ (blue dashed line) where μ'_s obtained from histopathology photomicrograph analysis for (a) insignificant lipid accumulation, (b) mild, (c) moderate and (d) severe lipid accumulation.

5.4 Lipid concentration in rat liver

The total area occupied by different graded steatosic liver with respect to microscopy result is presented in figure 5.9 (a). The severe steatotis group shows significantly higher (36.21±3.59) result compared to other steatosis groups. The control rats with the insignificant steatosis group showed a lipid area of 1.30±1.11. The area of lipid in the mild steatosis group (9.34±2.92) was higher than the insignificant group. The moderate stetosis group showed a lipid area of 21.94, which falls within the mild and severe steatotic group.

SfRS measurement of normalized intensity of different lipid accumulated liver at their day of euthanasia is presented in fig 5.9 (b). The mild accumulation, moderate and severe accumulation

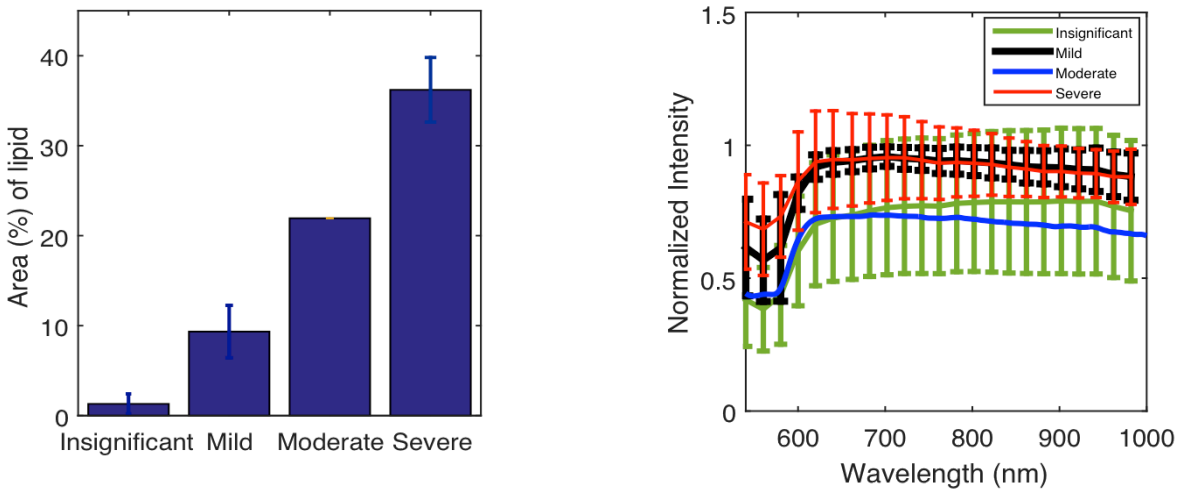

Figure 5.9: (a) Total area occupied by lipid vacuoles in microscopy images grouped by degree of lipid level, (b) measure SfRS normalized intensity grouped in degree of lipid level (green shows insignificant accumulation, black refers mild, blue refers moderate and red represents severe lipid accumulation)

group show a decreasing slope from 650nm-1000nm ranges, compared to the insignificant lipid accumulated liver group. There can also be seen a decreased absorption in the steatotic liver group at 540-650nm. A comparison of the SfRS normalized intensity trends in decreasing in slopes of the different steatosis accumulated liver groups relative to the insignificant steatosis

group, is presented in Fig 5.10 with their respective photomicrographs. The insignificant and mild steatosis accumulation rats were euthanized at day 13, insignificant and moderate rats were euthanized at day 27 and insignificant with severe steatotic liver rats were euthanized at day 55.

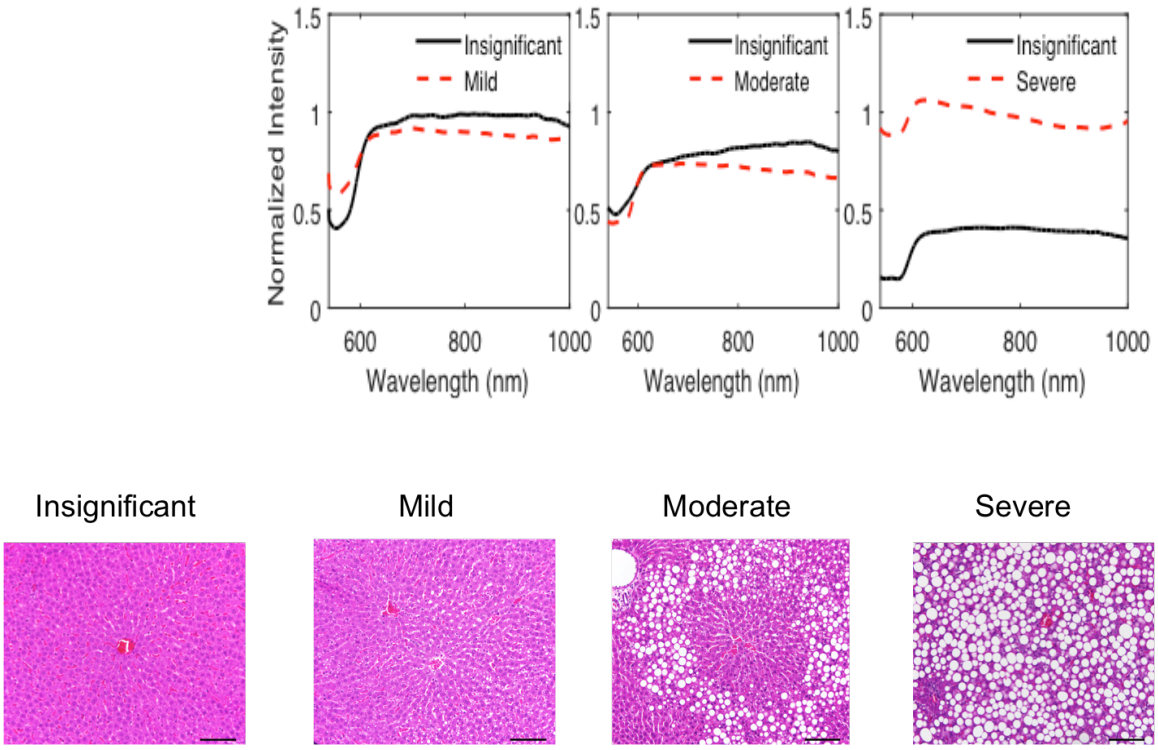

Figure 5.10: Comparison of SfRS intensity for steatotic liver with lean liver euthanized on same day presented as: Column (1): "insignificant" was from a control rat scarified on day 13. Column (2): "mild" was from a test rat and insignificant from control rat both scarified on day 13 Column (3): "moderate" was from a test rat and insignificant from control those scarified on day 27. Column (4): "severe" was from a test rat scarified on day 55 along with insignificant from control rat.

5.5 Total hemoglobin concentration

The estimated total hemoglobin concentration given in Fig. 5.11. The insignificant set contained the 4 rats originating from the control group and determined by histology to have lean livers. The four rats with histologically lean livers had a total hemoglobin concentration of 216.54±67.2

$1\mu M$ on their respective days of euthanasia. The three rats in the test group that had mild lipid accumulation as determined by histopathology were shown to have a total hemoglobin concentration of 148.32 ± 74.37 $1\mu M$. The moderate lipid accumulated liver had a total hemoglobin concentration of $128.87\ \mu M$. The four rats of the test group that all had severe steatotic livers had a total hemoglobin concentration of $77.33 \pm 34.97\ \mu M$ on their respective days of euthanasia.

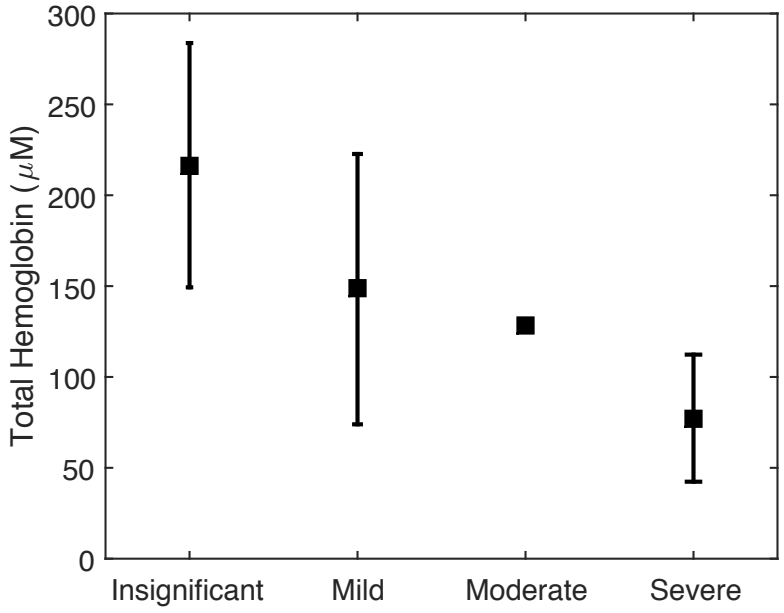

Figure 5.11: Total hemoglobin [HbT] of insignificant, mild, moderate and severe stetosis group measured on their day of euthanasia.

5.6 Scattering amplitude and scattering power

The scattering amplitude and scattering power are presented in Fig. 5.12 (a) and (b). The insignificant set contained the 4 rats scattering amplitude 0.06 ± 0.05 and scattering power 0.33 ± 0.0025 on their respective days of euthanasia. The three rats in the test set that had a mild

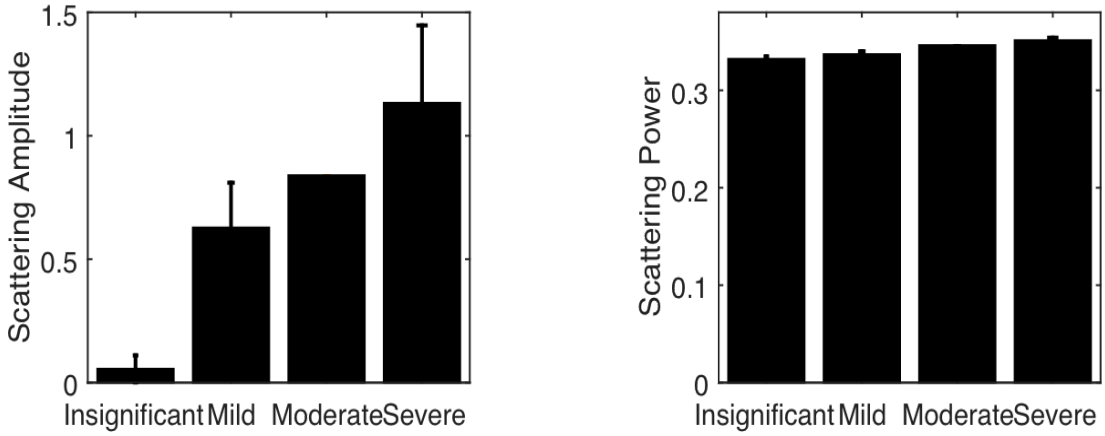

Figure 5.12: (a) Scattering amplitude and (b) scattering power measured from insignificant, mild, moderate and severe steatosis group at their respective day of euthanasia.

lipid accumulation as determined by histopathology shown scattering amplitude 0.63 ± 0.18 and scattering power 0.34 ± 0.0030. The moderate lipid accumulated liver group had a scattering amplitude 0.84 and scattering power 0.35. The four rats of the test group that all had severe steatotic livers show the scattering amplitude 1.13 ± 0.31 and scattering power 0.35 ± 0.0026 on their respective days of euthanasia.

CHAPTER VI

CONCLUSION

6.1 Conclusion

Rapid and objective assessment of the fatty changes of liver has implications for liver transplantation. The objective of this *in vivo* study was to evaluate if per-cutaneous single-fiber reflectance spectroscopy (SfRS) measurements respond to the onset of hepatic steatosis in rats induced by using a diet-based model.

This work represents single fiber reflectance spectroscopy (SfRS) and its analytical model depending on tissue probing geometry. Analytical modeling for calibration purpose has constructed for both infinite and semi-infinite probing of tissue geometry with respect to reference of having same geometry. The performance of this model compared with previous MC simulation studies, where surface probing was only considered. The normalization pattern of interstitial probing was also introduced here along with surface measurements were also introduced in our study. The behavior of normalization techniques were tested for a very low range of scattering co-efficient using intralipid where normalization technique of its respective geometry shows a more accurate pattern.

Animal studies have performed in a diet induced rat model utilizing a total of twelve rats, which included four control rats and eight test rats. This rat model study with this rat model continued

until day 55 having 5 iterations experiment with 14 day intervals between experimental evaluations. Photomicrograph of the livers from the twelve rats determined that four control rats euthanized respectively on day 13, 27, 41 and 55 had insignificant lipid accumulation, two test rats euthanized on day 13 and one test rat sacrificed on day 27 had mild lipid accumulation, one test rat euthanized on day 27 had moderate lipid accumulation, and four test rats euthanized respectively on day 41 and 55 had severe lipid accumulation.

The total area of lipid in microscopy image was obtained to validate the steatosis grading of the twelve rats. The severe steatosis group showed significantly higher lipid accumulation (36.21±3.59) results compared to the other steatosis groups. The control rats in the insignificant steatosis group showed a lipid area of 1.30±1.11. The area of lipid in the mild steatosis group (9.34±2.92) was higher than the insignificant group. The moderate steatosis group showed a lipid area of 21.94, which falls between the mild and severe steatotic groups.

The total hemoglobin concentration showed a decreasing trend while there was an increase in the level of steatosis present in rat liver. Lipid content in the liver had a detrimental impact on the total hemoglobin concentration detected. From a baseline of $216.54 \pm 67.2\ 1\mu M$ in the controls with an insignificant amount of lipid in their livers to total hemoglobin concentrations of $148.32 \pm 74.37\ 1\mu M$; $128.87\ \mu M$; and $77.33 \pm 34.97 \mu M$ for the mild, moderate and severely affected rat groups respectively.

The SfRS results for the 12 rats by their respective days of euthanasia were also compared to baseline values. There was a significant increase of scattering power between rats with histologically lean livers (0.33 ± 0.0025) and those with mild (34 ± 0.0030), moderate (0.35) and severe (0.35 ± 0.0026) steatotic livers at their days of euthanasia respectively.

6.2 Future works

The purpose of this study utilizing percutaneous single fiber reflectance spectroscopy performed on a rat model was to evaluate if SfRS could assess the potential change in fatty liver from normal liver. The performance of SfRS could be improved by using a broader wavelength spectrum source which colud reliably detect changes beyond 1000 nm.

The SfRS shows the potential to quantitatively determine the microstructure changes within the steatotic liver. As the lipid vacuole sizes increases, SfRS exhibits higher scattering amplitude and scattering power which can be related to higher scatter number density and larger scatter diameter. But to improve the calculation sensitivity in determining scattering power, more in depth studies need to be performed to investigate the relationship between the changes in reflectance spectrum and the microstructure changes in steatotic livers.

In the rat study reported here, the available images analyzed for this work are from H&E stained tissue, which include particles other than lipid present in the liver. Upon availability of the Oil Red O images, more accurate information of size distribution and number density of lipid particles could be obtained since they contain only lipid vacuoles, which could be useful in more accurately extracting tissue scattering properties more accurately.

The current analytical model of fiber probing geometry depending on the diffusion theory is based on isotropic scattering, thus being incapable of modeling the effect of anisotropic scattering phase function on the remission of photons for the case of SfRS. Recently a method [88] to accurately model photon diffusion near the point-of-entry in anisotropically scattering media was reported. Their approach decomposes the diffuse reflectance associated with a semi-infinite medium-boundary to one part resulting from diffusion approximation and a new part derived for correcting the anisotropic phase function. The phase function-dependent term of the photon fluence rate at a position of r_d (ρ,f,0) can be derived from [88] as:

$$R_{phase}^{z_a}(\rho) = \mu_s \left[p\left(-\frac{z_a}{\sqrt{\rho^2 + z_a^{\,2}}} \right) - \frac{1-g}{4\pi} \right] \exp\left[-\mu'_s \left(z_a + \sqrt{\rho^2 + z_a^{\,2}} \right) \right] \frac{z_a}{\left(\sqrt{\rho^2 + z_a^{\,2}} \right)^3}$$

where p is the actual phase function. It is therefore speculated that a term like Equation (2) that accounts for the anisotropic scattering would have the boundary effect built-in. Once such a boundary-effect term is identified, the contribution to the remission in different SfRS configurations by anisotropic scattering can be isolated according to the analytical procedures demonstrated in this work and possibly reaching a set of closed-form solutions [77].

REFERENCES

[1] Roberto Reif, Ousama A'Amar, and Irving J. Bigio, "Analytical model of light reflectance for extraction of the optical properties in small volumes of turbid media", Applied Optics, 46, (29), 7317-7328 (2007)

[2] S. C. Kanick, U. A. Gamm, M. Schouten, D. J. Robinson and A. Amelink, "Measurement of the reduced scattering coefficient of turbid media using single fiber reflectance spectroscopy: fiber diameter and phase function dependence", Biomedical Optics Express, 2, 6, 1687-1702 (2011).

[3] Kanick, S.C., Sterenborg, H.J.C.M., and Amelink, A., "Empirical model of the photon path length for a single fiber reflectance spectroscopy device", Opt. Express, 17(2): 860-871 (2009).

[4] Robert, L.P.v.V. and et al., "Optical biopsy of breast tissue using differential path- length spectroscopy", Physics in Medicine and Biology, 50(11): p. 2573 (2005).

[5] Bard, M.P.L., et al., "Measurement of Hypoxia-related Parameters in Bronchial Mucosa by Use of Optical Spectroscopy", Am. J. Respir. Crit. Care Med., 171(10): p. 1178-1184 (2005).

[6] Amelink, A., et al., "Non-invasive measurement of the morphology and physiology of oral mucosa by use of optical spectroscopy", Oral Oncol, 44(17350324): p. 65-71 (2008).

[7] Zonios, G., Bykowski, J., and lias, N., "Skin melanin, hemoglobin, and light scattering properties can be quantitatively assessed in vivo using diffuse reflectance spectroscopy", J Invest Dermatol, 17(11886508): p. 1452-1457 (2001).

[8] Chen, S.S., et al., "Measurement of redox states of mitochondrial cytochrome aa3 in regions of liver lobule by reflectance microspectroscopy", Am J Physiol, 264(8383443): p. 375-382 (1993).

[9] Koenig, F., et al., "Spectroscopic measurement of diffuse reflectance for enhanced detection of bladder carcinoma", Urology, 51(2): p. 342-345 (1998).

[10] Scientific Registry of Transplant Recipients, "2012 Annual Data Report", http://srtr.transplant.hrsa.gov/annual_reports/2012/flash/03_liver_13/v2index.html, accessed on Sep. 17 (2014).

[11] De Carlis L, Sansalone CV, Rondinara GF, Colella G, Slim AO, Rossetti O, Aseni P, Della Volpe A, Belli LS, Alberti A, Fesce R, Forti D, "Is the use of marginal donors justified in liver transplantation? Analysis of results and proposal of modern criteria," Transpl. Int. 9, S414–S417 (1996).

[12] Fishbein TM, Fiel MI, Emre S, Cubukcu O, Guy SR, Schwartz ME, Miller CM, Sheiner PA, "Use of livers with microvesicular fat safely expands the donor pool," Transplantation, 64, 248–251 (1997).

[13] Bigio, I.J. and Bown, S.G., "Spectroscopic sensing of cancer and cancer therapy: Current status of translational research", Cancer Biol. Ther., 3(3): p. 259- 267 (2004).

[14] Dehghani, H., et al., "Multiwavelength three-Dimensional Near-Infrared tomography of the breast: initial simulation, phantom, and clinical results", Appl. Opt., 42(1): p. 135-145 (2003).

[15] Piao, D., et al., "Alternative Transrectal Prostate Imaging: A Diffuse Optical Tomography Method. Selected Topics in Quantum Electronics", IEEE Journal 16(4): p. 715-729 (2010).

[16] Mourant, J.R., et al., "Spectroscopic diagnosis of bladder cancer with elastic light scattering. Lasers in Surgery and Medicine", 17(4): p. 350-357 (1995).

[17] Vo-Dinh, T., et al., "In vivo cancer diagnosis of the esophagus using differential normalized fluorescence (DNF) indices", Lasers in Surgery and Medicine, 16(1): p. 41-47 (1995).

[18] Kanick, S.C. and et al., "Monte Carlo analysis of single fiber reflectance spectroscopy: photon path length and sampling depth", Physics in Medicine and Biology, 54(22): p. 6991 (2009).

[19] Kanick, S.C., et al., "Integration of single-fiber reflectance spectroscopy into ultrasound-guided endoscopic lung cancer staging of mediastinal lymph nodes", Journal of Biomedical Optics, 15(1): p. 017004-8 (2010).

[20] F. van Leeuwen–van Zaane, U. A. Gamm, P. B. A. A. van Driel, T. J. A. Snoeks, H. S. de Bruijn, A. van der Ploeg–van den Heuvel, I. M. Mol, C. W. G. M. Löwik, H. J. C. M. Sterenborg, A. Amelink, and D. J. Robinson, "*In vivo* quantification of the scattering properties of tissue using multi-diameter single fiber reflectance spectroscopy", Biomedical Optics Express, Vol. 4, Issue 5, pp. 696-708 (2013).

[21] C. L. Hoy,U. A. Gamm, H. J. C. M. Sterenborg, D. J. Robinson, and A. Amelink, "Use of a coherent fiber bundle for multi-diameter single fiber reflectance spectroscopy", Biomed. Opt. Express 2452, Vol. 3, No. 10 (2012).

[22] T. P. Moffitt and S. A. Prahl, "Sized-fiber reflectometry for measuring local optical properties", IEEE J.S.T.Q.E., vol. 7, pp. 952–958 (2001).

[23] T. P. Moffitt and S. A. Prahl, "The Specular Reflection Problem with a Single Fiber for Emission and Collection" (2003).

[24] El-Desoky AE, Seifalian A, Cope M, Delpy D, Davidson B. "Changes in tissue oxygenation of the porcine liver measured by near-infrared spectroscopy", Liver TransplSurg 5(3):219 – 26 (1999).

[25] El-Desoky AE, Seifalian AM, Davidson BR, "Effect of graded hypoxia on hepatic tissue oxygenation measured by near infrared spectroscopy", J Hepatol. 31, 71–76 (1999).

[26] Yang BS, Ma YJ, Wang Y, Chen LY, Bi MR, Yan BZ, Bai L, Zhou H, Wang FX, "Protective effect and mechanism of stronger neominophagen C against fulminant hepatic failure," World J Gastroenterol. 13, 462–466 (2007).

[27] Seifalian AM, El-Desoky H, Delpy DT, Davidson BR, "Effect of graded hypoxia on the rat hepatic tissue oxygenation and energy metabolism monitored by near-infrared and 31P nuclear magnetic resonance spectroscopy," FASEB J. 15, 2642–2648 (2001).

[28] El-Desoky AE, Delpy DT, Davidson BR, Seifalian AM. "Assessment of hepatic ischaemia reperfusion injury by measuring intracellular tissue oxygenation using near infrared spectroscopy," Liver 21, 37–44 (2001).

[29] Nahum E, Skippen PW, Gagnon RE, Macnab AJ, Skarsgard ED, "Correlation of near-infrared spectroscopy with perfusion parameters at the hepatic and systemic levels in an endotoxemic shock model," Med Sci Monit. 12: BR313–317 (2006).

[30] Ohdan H, Mizunuma K, Tashiro H, Tokita D, Hara H, Onoe T, Ishiyama K, Shibata S, Mitsuta H, Ochi M, Nakahara H, Itamoto T, Asahara T, "Intraoperative near-infrared spectroscopy for evaluating hepatic venous outflow in living-donor right lobe liver," Transplantation 76, 791–797 (2003).

[31] Mitsuta H, Ohdan H, Fudaba Y, Irei T, Tashiro H, Itamoto T, Asahara T, "Near-infrared spectroscopic analysis of hemodynamics and mitochondrial redox in right lobe grafts in living-donor liver transplantation," Am J Transplant 6, 797–805 (2006).

[32] McLaughlin BL, Wells AC, Virtue S, Vidal-Puig A, Wilkinson TD, Watson CJ, Robertson PA, "Electrical and optical spectroscopy for quantitative screening of hepatic steatosis in donor livers," Phys Med Biol. 55(22), 6867-79 (2010).

[33] Gustavo Ribeiro De Oliveira, Ajith K. Sankarankutty, Orlando Castro e Silva , Juliana Ferreira, Cristina Kurachi, Sergio Zucoloto, Hélio Vannucchi, Alceu Afonso Jordão Jr, Júlio Sergio Marchini andVanderlei Salvador Bagnato, "Fluorescence spectroscopy to diagnose hepatic steatosis in a rat model of fatty liver", Volume 29, Issue 3, pages 331–336 (2009).

[34] Daniel J. Evers, Andrie C. Westerkamp, Jarich W. Spliethoff, Vishnu V. Pully, Daphne Hompes, Benno H. W. Hendriks, Warner Prevoo, Marie-Louise F. van Velthuysen,

Robert J. Porte and Theo J. M. Ruers, "Diffuse reflectance spectroscopy: toward real-time quantific ation of steatosis in liver", Transplant International, 28(4):465-74, (2015)

[35] Markin RS, Wisecarver JL, Radio SJ, Stratta RJ, Langnas AN, Hirst K, Shaw BW Jr, "Frozen section evalution of donor livers before transplantation", Transplantation, 56 (6)

[36] Ureña MA, Ruiz-Delgado FC, González EM, Segurola CL, Romero CJ, García IG, González-Pinto I, Gómez Sanz R., "Assessing risk of the use of livers with macro and microsteatosis in a liver transplant program", Transplant Proc., 30 (7), 3288-91.

[37] Joseph AE, Saverymuttu SH, "Ultrasound in the assessment of diffuse parenchymal liver disease", Clin Radiol. 44(4):219-21 (1991).

[38] Hamer OW, Aguirre DA, Casola G, Lavine JE, Woenckhaus M, Sirlin CB, "Fatty liver: imaging patterns and pitfalls", Radiographics, 26(6):1637-53 (2006).

[39] Charatcharoenwitthaya P, Lindor KD, "Role of radiologic modalities in the management of non-alcoholic steatohepatitis", Clin Liver Dis., 11(1): 37-54, viii (2007).

[40] Anneloes E. Bohte , Jochem R. van Werven, Shandra Bipat and Jaap Stoker, "The diagnostic accuracy of US, CT, MRI and ^{1}H-MRS for the evaluation of hepatic steatosis compared with liver biopsy: a meta-analysis", European Radiology, 21(1), 87-97 (2010).

[41] Zonios, G., et al., "Diffuse Reflectance Spectroscopy of Human Adenomatous Colon Polyps In Vivo", Appl. Opt. 38(31): p. 6628-6637 (1999).

[42] Friedland, S., et al., "Measurement of mucosal capillary hemoglobin oxygen saturation in the colon by reflectance spectrophotometry", GastrointestEndosc, 57(12665758): p. 492-497 (2003).

[43] Bhutani, V.K., et al., "Noninvasive measurement of total serum bilirubin in a multiracial predischarge newborn population to assess the risk of severe hyperbilirubinemia", Pediatrics, 106(10920173) (2000).

[44] Schenkman, K.A. and Yan, S., "Propofol impairment of mitochondrial respiration in isolated perfused guinea pig hearts determined by reflectance spectroscopy", Critical Care Medicine, 28(1): p. 172-177 (2000).

[45] Perelman, L.T., et al., "Observation of Periodic Fine Structure in Reflectance from Biological Tissue: A New Technique for Measuring Nuclear Size Distribution", Physical Review Letters, 80(3): p. 627 (1998).

[46] Wang, X., et al., "Approximation of Mie scattering parameters in near-infrared tomography of normal breast tissue in vivo", Journal of Biomedical Optics, 10(5): p. 051704-8 (2005).

[47] Fournell, A., et al., "Clinical evaluation of reflectance spectrophotometry for the

measurement of gastric microvascular oxygen saturation in patients undergoing cardiopulmonary bypass", Journal of Cardiothoracic and Vascular Anesthesia, 16(5): p. 576-581 (2002).

[48] Georgakoudi, I., et al., "Fluorescence, Reflectance, and Light-Scattering Spectroscopy for Evaluating Dysplasia in Patients With Barrett's Esophagus", Gastroenterology, 120(7): p. 1620-1629 (2001).

[49] Mirabal, Y .N., et al., "Reflectance spectroscopy for in vivo detection of cervical precancer", J Biomed Opt, 7(12421125): p. 587-594 (2002).

[50] Bigio, I.J., et al., "Diagnosis of breast cancer using elastic-scattering spectroscopy: preliminary clinical results", J Biomed Opt, 5(10938787): p.221-228 (2000).

[51] Breslin, T.M., et al., "Autofluorescence and diffuse reflectance properties of malignant and benign breast tissues", Ann SurgOncol, 11(14699036): p.65-70 (2004).

[52] Lin, W.-C., et al., "In Vivo Brain Tumor Demarcation Using Optical Spectroscopy", Photochemistry and Photobiology, 73(4): p. 396-402 (2001).

[53] Chen, S.S., et al., "Measurement of redox states of mitochondrial cytochrome aa3 in regions of liver lobule by reflectance microspectroscopy", Am J Physiol, 264(8383443): p. 375-382 (1993).

[54] Hoffmann, J., Lubbers, D.W., and Heise, H.M., "Applicability of the Kubelka-Munk theory for the evaluation of reflectance spectra demonstrated for haemoglobin-free perfused heart tissue", Phys. Med. Biol., 43(3571-3587) (1998).

[55] Müller, M.G., et al., "Spectroscopic detection and evaluation of morphologic and biochemical changes in early human oral carcinoma", Cancer, 97(7): p.1681-1692 (2003).

[56] Kollias, N. and Stamatas, G.N., "Optical non-invasive approaches to diagnosis of skin disease", J. Invest. Dermatol., 7: p. 64-75 (2002).

[57] Farrell, T.J., Patterson, M.S., and Wilson, B., "A diffusion theory model of spatially resolved, steady-state diffuse reflectance for the noninvasive determination of tissue optical properties in vivo", Medical Physics, 19(4): p. 879-888 (1992).

[58] Zonios, G. and Dimou, A., "Modeling diffuse reflectance from semi-infinite turbid media: application to the study of skin optical properties", Opt Express, 14(19529247): p. 8661-8674 (2006).

[59] Kim, A., et al., "A fiberoptic reflectance probe with multiple source-collector separations to increase the dynamic range of derived tissue optical absorption and scattering coefficients", Opt. Express, 18(6): p. 5580-5594 (2010).

[60] D. Piao, K. L. McKeirnan, Y. Jiang, M. A. Breshears, and K. E. Bartels, "A low-cost needle-based single-fiber spectroscopy method to probe scattering changes associated with mineralization in canine intervertebral disc," Photonics and Lasers in Medicine, 1(2): 103-115 (2012).

[61] S. C. Kanick, U. A. Gamm, H. J. C. M. Sterenborg, D. J. Robinson, and A. Amelink, "Method to quantitatively estimate wavelength-dependent scattering properties from multidiameter single fiber reflectance spectra measured in a turbid medium," Opt. Lett. 36, 2997-2999 (2011)

[62] U. A. Gamm, S. C. Kanick, H. J. C. M. Sterenborg, D. J. Robinson, and A. Amelink, "Quantification of the reduced scattering coefficient and phase-function-dependent parameter γ of turbid media using multidiameter single fiber reflectance spectroscopy: experimental validation," Opt. Lett. 37, 1838-1840 (2012).

[63] VirtualPhotonics Technology Initiative, http://www.virtualphotonics.org/software. Accessed on Nov. 5, 2014. This open source resource was made possible in part by the Laser Microbeam and Medical Program (LAMMP: P41 EB015890-33), an NIH/NIBIB Biotechnology Resource Center.

[64] Amelink, A. and Sterenborg, H.J.C.M., "Measurement of the Local Optical Properties of Turbid Media by Differential Path-Length Spectroscopy", Appl. Opt., 43(15): p. 3048-3054 (2004).

[65] Kaspers, O.P., Sterenborg, H.J.C.M., and Amelink, A., "Controlling the optical path length in turbid media using differential path-length spectroscopy: fiber diameter dependence", Appl. Opt., 47(3): p. 365-371 (2008).

[66] J. R. Mourant, T. M. Johnson, G. Los, and I. J. Bigio, "Non-invasive measurement of chemotherapy drugconcentrations in tissue: preliminary demonstrations of in vivo measurements," Phys. Med. Biol. 44, 1397–1417 (1999).

[67] M. Canpolat and J. R. Mourant, "Monitoring photosensitizer concentration by use of a fiber-optic probe with small source-detector separation," Appl. Opt. 39, 6508–6514 (2000).

[68] van Staveren, H.J., et al., Light scattering in Intralipid-10% in the wavelengthrange of 400-1100 nm. Appl. Opt., 30(31): p. 4507-4514 (1991).

[69] Pogue, B.W., et al., "Quantitative hemoglobin tomography with diffuse nearinfrared spectroscopy: pilot results in the breast", Radiology, 218(11152812): p. 261-266 (2001).

[70] Mourant, J.R., et al., "Predictions and measurements of scattering and absorptionover broad wavelength ranges in tissue phantoms", Appl Opt, 36(18250760): p. 949-957 (1997).

[71] Srinivasan, S., et al., "Interpreting hemoglobin and water concentration, oxygen

saturation, and scattering measured in vivo by near-infrared breast tomography", Proceedings of the National Academy of Sciences of the United States of America, 100(21): p. 12349- 12354 (2003).

[72] Hoy CL, Gamm UA, Sterenborg HJ, Robinson DJ, Amelink A., "Method for rapid multidiameter single-fiber reflectance and fluorescence spectroscopy through a fiber bundle", J Biomed Opt., 18(10):107005. JBO.18.10.107005 (2013).

[73] K. M. Case and P. F. Zweifel, Linear Transport Theory (Addison-Wesley, Reading, Mass., Sec. 1.3 (1967).

[74] J. J. Duderstadt and L. J. Hamilton, Nuclear Reactor Analysis (Wiley, New York, 1976).

[75] B. Davison, Neutron Transport Theory (Oxford, London,1958). Haskell et al. Vol. 11, No. 10/October 1994/J. Opt. Soc. Am.A 2741.

[76] S. Glasstone and M. C. Edlund, The Elements of Nuclear Reactor Theory (Van Nostrand, Princeton, N.J., 1952), Chaps. 5and 14.

[77] Daqing Piao and Joel W. Slaton, "Single-Fiber Reflectance Spectroscopy of Isotropic-Scattering Medium: An Analytic Perspective to the Ratio-of-Remission in Steady-State Measurements", Photonics, 1, 565-585, (2014).

[78] R. C. Haskell, L. O. Svaasand, T. Tsay, T. Feng, M. S. McAdams, and B. J. Tromberg, "Boundary conditions for the diffusion equationin radiative transfer," J. Opt. Soc. Am. A 11, 2727–2741 (1994).

[79] D. Contini, F. Martelli, and G. Zaccanti, "Photon migration through a turbid slab described by a model based on diffusion approximation. I. Theory," Appl. Opt. 36, 45874599 (1997).

[80] A. Da Silva, M. Leabad, C. Driol, T. Bordy, M. Debourdeau, J. Dinten, P. Peltié, and P. Rizo, "Optical calibration protocol for an x-ray and optical multimodality tomography system dedicated to small-animal examination," Appl. Opt. 48, D151–D162 (2009).

[81] R. Aronson, "Boundary conditions for diffusion of light," J. Opt.Soc.Am.A 12, 2532-2539 (1995).

[82] Martelli F, Zaccanti G. Calibration of scattering and absorption properties of a liquid diffusive medium at NIR wavelengths. CWmethod. Opt Express; 15(2):486 – 500 (2007).

[83] Chui, A. K., Haghighi, K., Painter, D. et al. Donor fatty (steatotic) liver allografts in orthotopic liver transplantation. Transplant Proc. 30, 3286–3287 (1998).

[84] Matcher, S.J., Winlove, C.P., and Gangnus, S.V., The collagen structure of bovine intervertebral disc studied using polarization-sensitive optical coherence tomography. Phys Med Biol, 2004. 49(15128206): p. 1295-1306.

[85] Wang, L.V., *Biomedical Optics: Principles and Imaging*. 1st ed. 2007: Wiley-

Interscience. 376.

[86] Weast, R.C. and Lide, D.R., *Handbook of Chemistry and Physics*. 67th ed. 1986: Chemical Rubber Company.

[87] Evers DJ, Nachabé R, Hompes D, van Coevorden F, Lucassen GW, Hendriks BH, van Velthuysen ML, Wesseling J, Ruers TJ, "Optical sensing for tumor detection in the liver", Eur J Surg Oncol., 39(1):68-75 , (2013).

[88] Vitkin, E.; Turzhitsky, V.; Qiu, L.; Guo, L.; Itzkan, I.; Hanlon, E.B.; Perelman, L.T. Photon diffusion near the point-of-entry in anisotropically scattering turbid media. Nat. Commun, 13, 587 (2011).

APPENDICES

Matlab programs

Mie Theory

```
diameter=input(diameter of sphere);
radius=diameter/2;
lambda= input(wavelength);
n_s= input(refractive index of sphere);
n_b= input(refractive index of background);
w_s= input(specific weight of sphere);
w-b= input(specific weight of background);
concentration= input(concentration by weight);

k=2.*pi.*n_b./lambda;
    x=k.*radius;
    n_rel=n_s/n_b;
    y=n_rel.*x;
    err=1e-8;
Qs=0;
gQs=0;
for n=1:100000
    Snx=sqrt(pi.*x/2).*besselj(n+0.5,x);
    Sny=sqrt(pi.*y/2).*besselj(n+0.5,y);
    Cnx=-sqrt(pi.*x/2).*bessely(n+0.5,x);
    Zetax=Snx+i*Cnx;

    Snx_prime=-(n./x).*Snx+sqrt (pi.*x/2).*besselj(n-0.5,x);
    Sny_prime=-(n./y).*Sny+sqrt(pi.*y/2).*besselj(n-0.5,y);
    Cnx_prime=-(n./x).*Cnx-sqrt(pi.*x/2).*bessely(n-0.5,x);
    Zetax_prime=Snx_prime+i*Cnx_prime;

    an_num=Sny_prime.*Snx-n_rel.*Sny.*Snx_prime;
    an_den=Sny_prime.*Zetax-n_rel.*Sny.*Zetax_prime;
    an=an_num./an_den;

    bn_num=n_rel.*Sny_prime.*Snx-Sny.*Snx_prime;
    bn_den=n_rel.*Sny_prime.*Zetax-Sny.*Zetax_prime;
    bn=bn_num./bn_den;

    Qs1=(2.*n+1).*(abs(an).^2+abs(bn).^2);
```

```
Qs=Qs+Qs1;

    if n>1
        gQs1=(n-1).*(n+1)./n.*real(an_1.*conj(an)+bn_1.*conj(bn))
            +(2.*n-1)/((n-1).*n).*real(an_1.*conj(bn_1));
        gQs=gQs+gQs1;
    end

    an_1=an;
    bn_1=bn;
    if abs(Qs1)<(err*Qs) & abs(gQs1)<(err*gQs);
        break;
    end
end

Qs=(2./x.^2).*Qs;
gQs=(4./x.^2).*gQs;
g=gQs./Qs;

% Output
sigma_s=Qs.*pi.*radius.^2;
mu_s=N_s.*sigma_s;
mu_s_prime=mu_s_prime+mu_s.*(1-g)/1000;
lamda=lambda*10^9;
end
```

Image processing

```
originalimage = imread('image.tif');
I = rgb2gray(originalimage);
bI=im2bw(I,0.85);
imshow(bI);
```

Size distribution

```
labeledImage = bwlabel(bI);
measurements = regionprops(labeledImage, 'EquivDiameter');
allDiameters = [measurements.EquivDiameter];
numberOfBins = n;
[diamDistribution binDiameters] = hist(allDiameters,
numberOfBins);
```

VITA

NIGAR SULTANA

Candidate for the Degree of

Master of Science

Thesis: IN-VIVO PER-CUTANEOUS SINGLE FIBER REFLECTANCE SPECTROSCOPY OF HEPATIC STEATOSIS IN A RAT MODEL: QUANTITATIVE ASSESSMENT WITH RESPECT TO HISTOPATHOLOGY

Major Field: Interdisciplinary science (Electrical and Computer Engineering)

Biographical: Born in Dhaka, Bangladesh on December 29, 1988.

Education:

Received the Bachelor of Science in Electrical, Electronic and Communication Engineering at Military Institute of Science and Technology, Dhaka, Bangladesh in 2010.

Experience:

Research Assistant
Optical Imaging Lab, ECE Department
Oklahoma State University
(Jan, 2013-Dec, 2015)

Senior System Engineer,
Grameenphone, Dhaka Bangladesh
(Aug, 2010-Dec, 2012)